

AD-A196 952

47691-6002-UT-00

Modulation of Radar Backscatter from the Ocean
by a Variable Surface Current

by

E. A. Caponi
D. R. Crawford
H. C. Yuen
P. G. Saffman*

June 27, 1988

Prepared for:

Office of Naval Research
Contract No. N00014-86-C-0111

Approved for public release, unlimited distribution

TRW Space & Technology Group
One Space Park
Redondo Beach, California 90278

*California Institute of Technology, Pasadena, CA 91125

DTIC
ELECTE
JUN 28 1988
S D
H

88 6 28 163

UNCLASSIFIED

SECURITY CLASSIFICATION OF THIS PAGE

REPORT DOCUMENTATION PAGE

1a. REPORT SECURITY CLASSIFICATION Unclassified			1b. RESTRICTIVE MARKINGS		
2a. SECURITY CLASSIFICATION AUTHORITY			3. DISTRIBUTION/AVAILABILITY OF REPORT Approved for public release, distribution unlimited		
2b. DECLASSIFICATION/DOWNGRADING SCHEDULE					
4. PERFORMING ORGANIZATION REPORT NUMBER(S) 47691-6002-UT-00			5. MONITORING ORGANIZATION REPORT NUMBER(S) -		
6a. NAME OF PERFORMING ORGANIZATION Fluid Mechanics Department TRW Space & Technology Group		6b. OFFICE SYMBOL (If applicable) R1/1008	7a. NAME OF MONITORING ORGANIZATION		
6c. ADDRESS (City, State, and ZIP Code) One Space Park Redondo Beach, California 90278			7b. ADDRESS (City, State, and ZIP Code)		
8a. NAME OF FUNDING/SPONSORING ORGANIZATION Office of Naval Research		8b. OFFICE SYMBOL (If applicable)	9. PROCUREMENT INSTRUMENT IDENTIFICATION NUMBER		
8c. ADDRESS (City, State, and ZIP Code) Department of the Navy 800 North Quincy Street Arlington, VA 22217-5000			10. SOURCE OF FUNDING NUMBERS		
			PROGRAM ELEMENT NO.	PROJECT NO.	TASK NO.
			WORK UNIT ACCESSION NO.		
11. TITLE (Include Security Classification) Modulation of Radar Backscatter from the Ocean by a Variable Surface Current					
12. PERSONAL AUTHOR(S) E. A. Caponi, D. R. Crawford, H. C. Yuen, P. G. Saffman					
13a. TYPE OF REPORT Final (2 of 2)		13b. TIME COVERED FROM 1/1/86 TO 6/27/88	14. DATE OF REPORT (Year, Month, Day) June 27, 1988		15. PAGE COUNT 66
16. SUPPLEMENTARY NOTATION					
17. COSATI CODES			18. SUBJECT TERMS (Continue on reverse if necessary and identify by block number)		
FIELD	GROUP	SUB-GROUP	Radar Backscatter, Surface Wave Modulations, Wave-Current Interactions, Georgia Strait Experiment, JOWIP. (RPT) 17		
19. ABSTRACT (Continue on reverse if necessary and identify by block number) Calculations of surface wave and radar cross section modulation induced by a spatially varying surface current have been compared with field measurements made with SAR (X- and L-bands), real aperture radar (X-band), laser slope gauge, and CCD video camera during the Joint Canada/U.S. Ocean Wave Investigation Project (JOWIP) which took place in August 1983. The comparison reveals that (i) many existing wind-relaxation models underpredict the hydrodynamic effect of the current, (ii) simple Bragg scattering model underpredicts radar backscatter modulation for higher frequency radars (e.g., X-band) but appears acceptable at lower radar frequencies (e.g., L-band), (iii) the discrepancy between measurements and calculations at high radar frequency is reduced, but not eliminated, when the effects of long surface waves have been accounted for,					
20. DISTRIBUTION/AVAILABILITY OF ABSTRACT <input type="checkbox"/> UNCLASSIFIED/UNLIMITED <input checked="" type="checkbox"/> SAME AS RPT. <input type="checkbox"/> DTIC USERS			21. ABSTRACT SECURITY CLASSIFICATION UNCLASSIFIED		
22a. NAME OF RESPONSIBLE INDIVIDUAL			22b. TELEPHONE (Include Area Code)		22c. OFFICE SYMBOL

DD FORM 1473, 84 MAR

83 APR edition may be used until exhausted
All other editions are obsolete.

SECURITY CLASSIFICATION OF THIS PAGE

UNCLASSIFIED

MODULATION OF RADAR BACKSCATTER
FROM THE OCEAN BY A VARIABLE SURFACE CURRENT.

by

E. A. Caponi, D. R. Crawford, H. C. Yuen,
Fluid Mechanics Department, TRW Space and Technology Group,
One Space Park, Redondo Beach, CA 90278,

and

P. G. Saffman,
Applied Mathematics, California Institute of Technology,
Pasadena, CA 91125.

Accession For	
NTIS GRA&I	<input checked="" type="checkbox"/>
DTIC TAB	<input type="checkbox"/>
Unannounced	<input type="checkbox"/>
Justification	
By _____	
Distribution/	
Availability Codes	
Dist	Avail and/or Special
A-1	

ABSTRACT

Calculations of surface wave and radar cross section modulation induced by a spatially varying surface current have been compared with field measurements made with SAR (X- and L- bands), real aperture radar (X-band), laser slope gauge, and CCD video camera during the Joint Canada/U.S. Ocean Wave Investigation Project (JOWIP) which took place in August 1983. The comparison reveals that (i) many existing wind-relaxation models underpredict the hydrodynamic effect of the current, (ii) simple Bragg scattering model underpredicts radar backscatter modulation for higher frequency radars (e.g., X-band) but appears acceptable at lower radar frequencies (e.g., L-band), (iii) the discrepancy between measurements and calculations at high radar frequency is reduced, but not eliminated, when the effects of long surface waves have been accounted for.



1. INTRODUCTION

One of the major objectives in the Joint Canada/U.S. Ocean Wave Investigation Project (JOWIP) was the evaluation of the capabilities and limitations of theoretical models for predicting the modulation of real and synthetic aperture radar backscatter from the ocean by a variable surface current induced by internal waves, flow over bottom topography, or other wavelike or non-wavelike disturbance.

JOWIP, or the Georgia Strait experiment as it is commonly known in the community, has the potential of making a substantial contribution to the understanding of ocean physics and its remote sensing by synthetic aperture radar (SAR) in that the *X*- and *L*-band simultaneous airborne SAR measurements are supported by a full set of ground truth measurements, providing *in situ* measurements of subsurface characteristics (CDT profiles), surface characteristics (*x-y* current, wind velocity, surface wave slope), real aperture radar returns (*X*-band radar supported by optical specular detector), optical returns (CCD video camera), stereo photographs, and airborne photographs. The SAR overflights and ship crossings are co-ordinated, synchronized and tracked.

The wealth of quantitative ground truth data taken during SAR overflights makes JOWIP uniquely qualified to validate and assess a theoretical model. Measurements of surface current, surface wave slope, and real aperture radar (RAR) backscatter provide all of the data needed to test each of the major components in such a model. The JOWIP data collection, unlike for example, SARSEX data which lacks direct surface current measurements and real aperture radar data, can be used to test the hydrodynamic model by comparing with the current and wave slope data, the radar scattering model by comparing with the wave slope and RAR backscatter data, and the radar imaging model by comparing with the wave slope, RAR and SAR data. Without these intermediate tests of the components, the large number of variables in an end-to-end SAR simulation model makes it all too easy to improperly attribute successes or failures of one component to another, or to arrive at misleading conclusions due to cancelling effects of simplifications made within different components.

In this paper, we test the models for (a) hydrodynamic interaction of a surface wind wave field with surface currents, (b) radar scattering from the modulated surface waves. We compare results of model calculations obtained with the TRW Hydrodynamic Interaction Code (TRW-HIC) to remote measurements obtained by synthetic aperture radar (SAR) and to surface measurements obtained by ship-borne slope gauge and real aperture CW radar (RAR). The comparison focuses on the validity of several important elements of the theoretical model:

- a. The model for wind effects (relaxation model);
- b. The model for the equilibrium spectrum in the absence of a variable surface current;
- c. The effects of certain simplifying assumptions in the model;
- d. The Bragg model for radar backscatter;
- e. The long wave field effects.

Computations were made for a number of runs to address the above issues. Two cases (JOWIP 1-1 and TRW 81B), were selected for detailed quantitative comparisons.

Shortly after the completion of the work reported here, a new radar ocean imaging model was proposed by Holliday *et al* (1986). Comparison between the results presented here and results obtained by using this new model will be the subject of a following paper.

2. MODEL FOR BRAGG WAVE MODULATION BY A VARIABLE CURRENT

The Bragg model proposes that the backscatter of electromagnetic radiation from the ocean surface is mainly due to waves of a specific wavelength through a grating like mechanism. For a radar with wave number k_r and incidence angle θ , the model predicts that only water waves of wavenumber $k_B = 2k_r \sin \theta$ in the line of sight contribute to the backscatter. The radar cross section σ is predicted by the Bragg model to be proportional to $F(\vec{k}_B)$, where F is the spectral density function of water waves (Wright, 1966). The model assumes a spatially homogeneous wave field, and for sufficiently steady conditions, F is given by the equilibrium wave-height distribution $F_{eq}(\vec{k})$ for the prevailing wind (see, for example, Pierson and Stacy, 1973).

A straightforward extension of the model to the case where the surface wave spectrum is spatially modulated by a variable surface current $\vec{U}(\vec{x}, t)$ allows the identification of relative spatial changes in backscatter cross section with relative spatial changes in the spectral content at the Bragg resonant wavenumber. If a dimensionless spectral density perturbation function $f(\vec{k}, \vec{x}, t)$ associated with $\vec{U}(\vec{x}, t)$ is defined as

$$(1) \quad f(\vec{k}, \vec{x}, t) = \frac{F(\vec{k}, \vec{x}, t) - F_{eq}(\vec{k})}{F_{eq}(\vec{k})},$$

then to leading order, the modulated radar cross section due to backscatter in the

presence of the current is

$$(2) \quad \sigma(\vec{k}_B, \vec{z}, t) = \sigma_0(\vec{k}_B) [1 + f(\vec{k}_B, \vec{z}, t)],$$

where $\sigma_0(\vec{k}_B)$ is the steady state Bragg backscatter cross section in the absence of a surface current. The relative modulation of the backscatter cross section is then the nondimensional perturbation in the surface wave spectrum of the Bragg wave component:

$$\frac{\Delta\sigma(\vec{k}_B, \vec{z}, t)}{\sigma_0(\vec{k}_B)} = f(\vec{k}_B, \vec{z}, t).$$

A. Governing Equations.

In the absence of source terms (including wind energy input and dissipation), the local wave action $N(\vec{k}, \vec{z}, t)$ is conserved. In the presence of wind, N obeys the equation:

$$(3) \quad \frac{dN}{dt} = \frac{\partial N}{\partial t} + \vec{\nabla}_z N \cdot \frac{d\vec{z}}{dt} + \vec{\nabla}_k N \cdot \frac{d\vec{k}}{dt} = S_W,$$

where S_W models the effect of wind. The ray trajectories are given by

$$(4) \quad \frac{d\vec{z}}{dt} = \frac{\partial \omega}{\partial \vec{k}},$$

$$(5) \quad \frac{d\vec{k}}{dt} = -\frac{\partial \omega}{\partial \vec{z}},$$

where

$$(6) \quad \omega = \omega' + \vec{k} \cdot \vec{U}(\vec{z}, t)$$

is the local dispersion relation, and ω' is the intrinsic frequency given by

$$(7) \quad \omega'^2 = gk(1 + Tk^3),$$

with T the surface tension coefficient, and $k = |\vec{k}|$.

The action density $N(\vec{k}, \vec{z}, t)$ is related to the spectral density function $F(\vec{k}, \vec{z}, t)$ by the relation

$$(8) \quad N(\vec{k}, \vec{z}, t) = \frac{\omega'}{k} F(\vec{k}, \vec{z}, t).$$

In the absence of a current pattern, the surface wave field is assumed to be established by a constant wind blowing for a long time, and is described by a spatially homogeneous equilibrium spectral density function $F_{eq}(\vec{k})$, which is determined heuristically.

The wind source term S_W is assumed to take the form

$$(9) \quad S_W = \beta \frac{\omega'}{k} F \left[1 - |F/F_{eq}|^\alpha \right],$$

where α can be 1 or 2 depending on whether the restoring force is quadratic or cubic. This source term acts to (a) develop a flat surface into the equilibrium spectrum under a given wind, and (b) restore any departure from this equilibrium, at the same rate; this "relaxation" rate β being a function of wind and wavelength. The relaxation rate β is also determined heuristically, based mainly on wave growth data in the laboratory and the ocean (cf. Section 2Bb).

The surface current $\vec{U}(\vec{z}, t)$ is taken to be a steady pattern propagating in the x direction with a speed V . In the frame of reference moving with V , the current pattern is described by $\vec{U}(\vec{z}^*) = \vec{U}(x - Vt, y)$, and the resultant spatially inhomogeneous equilibrium spectral density function can be written in terms of F_{eq} and of the dimensionless spectral perturbation f defined in Equation (1) and evaluated at (\vec{k}, \vec{z}^*) . (Henceforth, we will drop the $*$ when the context is clear).

Incorporating Equations (1), (8) and (9) into Equation (3) yields the evolution equation for $f(\vec{k}, \vec{z})$

$$(10) \quad \frac{df}{dt} = -(1+f) \left[\beta f \left(\alpha + \frac{\alpha-1}{2} f \right) + \frac{1}{k} \frac{d\vec{k}}{dt} \cdot \frac{\partial \vec{k}}{\partial \vec{k}} \left(\frac{k}{\omega} \frac{\partial \omega}{\partial \vec{k}} - 1 + \frac{k}{F_{eq}} \frac{\partial F_{eq}}{\partial \vec{k}} \right) \right].$$

According to the Bragg scattering model, the solution of Equation (10) along the wave trajectories defined by Equations (4) and (5), gives the relative changes in backscatter cross section for a given wind and a given surface current distribution.

B. Modeling issues.

The approach described above requires that the current pattern propagation and the wind conditions be reasonably steady. Assuming this to be fulfilled in the cases where the model is applied,

there are several issues that are relevant to the validity of the model.

a. Model for Equilibrium Spectrum.

In the case of the Georgia Strait experiments, preliminary comparison with background slope gauge measurements indicated that the Pierson-Stacy (1973) model is in reasonable agreement with data in the energy-containing part of the spectrum. Based on that comparison, this equilibrium spectrum was used in the calculations presented here. Detailed comparisons in the high wavenumber range and on directional dependence have not been made.

b. Model for the Wind Source Term and Relaxation Rate.

There are several primarily heuristic models available for the relaxation rate β . They are based mainly on different sets of wave growth data in the laboratory and in the ocean, with some overlapping in the parameter regime. Models that we have implemented are:

- a. Inoue (1966) model,
- b. Miles (1959) model,
- c. Snyder and Cox (1966) model,
- d. Snyder *et al* (1981) model,
- e. Mitsuyasu and Honda (1982) model,
- f. Hughes (1978) model,
- g. Plant (1982) model.

The first five models listed are to be used with a cubic restoring force in the wind source term (i.e., $\alpha=2$ in Equation (9)), while the last two models are for a quadratic ($\alpha=1$) restoring force. In all of these models, for a given wind, the shorter waves have a larger relaxation rate (shorter relaxation time). Hence, they are more responsive to wind action. However, the actual values for β are spread over an order of magnitude among the different models, as illustrated in Figure 1.a for the case of a 5 m/sec wind. Also, there is presently no reliable data to support any specific directional dependence in β .

For a given wind speed, the Inoue model gives the largest relaxation rate, thus the strongest wind effect. When compared with the Snyder *et al* (1981) model (labelled "Sea" in Figure 1.a), Inoue's model has a relaxation rate about one order of magnitude larger, and hence predicts a modulation about one order of magnitude smaller. A sample of results obtained using various β models is shown in Figure 1.b.

Preliminary comparison with Georgia Strait data clearly indicated that calculations using the Inoue model were underpredicting the measurements. For this reason, the model yielding the largest perturbation - which is the Snyder *et al* (1981) model - was selected over the Inoue (1967) model. This selection has been confirmed by detailed comparison. The Hughes (1978) model, when used in conjunction with a quadratic restoring force term (which effectively reduces the relaxation rate by a factor of 2 for small departures from equilibrium), yields results comparable to the Snyder *et al* model for small modulations.

When applied to the prevailing conditions of these experiments, the various β models would have produced results spread over a range larger than one order of magnitude. The selection of the Snyder *et al* (and Hughes) models over the Inoue model is a very important conclusion from the JOWIP data. It implies that previous calculations which used the Inoue model may have underpredicted surface modulations induced by internal waves by up to an order of magnitude. However, it should be pointed out that this, as many of the other conclusions, is based on a limited number of cases analysed. More data (including JOWIP data not yet processed) should be analysed to fortify or challenge a conclusion as important as this.

c. Simplifying Assumptions.

Several popular approaches to the solution of Equation (10) involve further simplifications. We make a few observations about the effect of some of these simplifications in the application to the Georgia Strait experiments.

i) Linearization about the Equilibrium Spectrum.

When the current and its variations are small, the induced perturbations are also expected to be small. The *a priori* assumption that $f \ll 1$ justifies linearization of the equation about the equilibrium spectrum. Instead of solving Equation (10) which is nonlinear in f , the governing equation becomes:

$$(11) \quad \frac{df}{dt} = -\alpha\beta f + \frac{\partial U}{\partial x} \left[\frac{k}{\omega} \frac{\partial \omega}{\partial k} - 1 + \frac{k}{F_{eq}} \frac{\partial F_{eq}}{\partial k} \right].$$

Comparison between the full and linearized calculations for surface currents corresponding to the Georgia Strait experiment show good agreement for those portions of the record where current gradients are very weak. However, where the modulation f is not very small, say larger than 10%, the

solution to the linearized equation departs considerably from that of the full equation, leading in many cases to unphysical negative values for the spectral density F (i.e., $f < -1$).

ii) Linearized Characteristics.

Another simplification is to employ straight characteristics rather than curved characteristics when integrating the spectral equation. The validity of this assumption can be pre-tested by plotting the characteristics before performing the calculations. An example of such a plot for JOWIP 1-1 is shown in Figure 2. It can be seen that in certain wavenumber ranges, the waves are actually "trapped" by the current pattern. For both L - and X -band, the characteristics are strongly curved, indicating that the straight-characteristics assumption fails for this case.

iii) Beta-Dominant Approximation.

The so-called "beta-dominant" approximation assumes that the wind restoration mechanism is dominant in the sense that it restores the wave spectrum to a new equilibrium instantaneously. This assumption leads (Alpers and Hennings, 1984) to

$$(12) \quad f = - \frac{4.5}{\alpha\beta} \frac{\partial U}{\partial x}.$$

The simplicity of the expression makes this a popular means for obtaining a "first estimate" on the modulational magnitude.

Since the wind relaxation rate β increases with decreasing wavelength, this approximation is expected to become applicable as the waves of interest become appropriately short. This is supported by comparison with results obtained with the full equations. For example, in the case of JOWIP 1-1, the beta-dominant approximation fails at L -band, yielding results 3 times larger than those from the full equations, and producing negative spectral density values. For X -band, the beta dominant approximation is acceptable, yielding results about 20% larger than those obtained from the full equations.

If the Inoue relaxation model (which has a β value one order of magnitude larger) were used, then the beta-dominant solutions approximate the solutions of full equations well for this data set — both being about an order of magnitude smaller than the results using the Snyder *et al* model. This suggests that the apparent success attributed to the beta-dominant approximation in the past was the result of adopting a large β -value model. With the selection of the Snyder *et al* model over the Inoue model, the acceptability of the beta-dominant approximation has been greatly reduced.

C. TRW-HIC Implementation.

Our implementation allows the user to specify the desired equilibrium wind wave spectrum, to choose among any of the relaxation rate models listed in Section 2Ab, to use either a quadratic or a cubic wind restoration term, and to impose any of the additional simplifying assumptions listed in Section 2Ac.

The main output is the dimensionless spectral perturbation $f(\vec{k}, \vec{x})$, from which the full spectrum can be reconstructed and root-mean-square wave height and wave slope obtained. Additionally, these hydrodynamic disturbances can then be converted into sensor responses: radar cross-section modulation, surface glitter pattern, surface imagery of sky reflection, and geometric effects on radiometric returns.

For the results presented in this paper, the Pierson-Stacy spectrum was used. Also, we have chosen the wind restoration term to be cubic [i.e., $\alpha=2$ in Equation (9)]. Given the evidence referred to in Section 2Bb, the relaxation rate was chosen to be as given by Snyder *et al* (1981). For consistency, β 's angular dependence was taken to be the same as in the Pierson-Stacy spectrum.

None of the simplifying assumptions of Section 2Bc was exercised in the generation of the results presented here. However, due to the favorable conditions of the cases chosen, the unidirectional version of the code was used.

3. APPLICATION TO GEORGIA STRAIT EXPERIMENTS.

A. Geometric Considerations.

The DREP current meters, the DREP slope gauge, the APL video camera and the TRW X-band CW RAR are all ship mounted. These measurements comprise the set of ground-truth data along a trajectory traversed by the ship. These ship-borne instruments, however, do not measure the exact same spot of water surface.

The ERIM SAR provides an area image. A cut in the SAR image, colocated with the ship trajectory to the extent possible, is used for comparisons with other measurements and with calculations.

The calculated results of spectral perturbation at the Bragg resonant wavenumber are compared with the slope gauge output bandpassed around the Bragg component, the X-band real aperture result (when available), the video data (when available) and the SAR cut. To the extent that these various output measurements are not spatially or temporally colocated, there is some intrinsic uncertainty in the comparison itself which must be borne in mind by the reader.

The input quantities for a calculation are:

- a. Wind speed and direction (from meteorological package),
- b. Current magnitude and direction (from current meter),
- c. Current pattern propagation speed and direction (both from delays between bow and stern current meters and from consecutive SAR images).

These vectors are resolved in the direction of the ship motion. The calculations are therefore unidirectional along the ship track.

B. Quantitative Comparison with Data.

Based on a quick-look analysis, several runs were selected for detailed data processing, including JOWIP 1-1, 12-3/4, 14-4, 15-7 and TRW 81B, all of which are for currents induced by naturally occurring internal waves. Among the most important selection criteria were the availability of good data and the distinctive characteristic of the internal wave signals. Calculations were performed for all these cases. Quantitative comparisons with measurements were made to the extent possible. In the following, detailed comparisons between calculations and data are shown for JOWIP 1-1 and TRW 81B only; however, the general conclusions are supported by the other cases examined.

a. JOWIP RUN 1-1.

This run corresponds to data taken between 17:44:31 and 18:26:19 PDT on July 22, 1983. In this case, the wind speed was recorded at 10 m height as 3.4 m/s blowing toward 95°T. The ship was heading 98°T at an approximately constant speed of 1 m/s. The ship crossed a pattern of internal waves associated with a shallow and sharp thermocline with a maximum Brunt-Väisälä frequency of 60 cycle per hour at a depth of 2.5 m. The surface current as a function of distance along the track is shown in Figure 2a. The propagation direction of the pattern was determined from the SAR images to be about 110°T, and the speed from the time delay between bow and stern current meters to be 0.01 m/s. (Velocities are all land referenced.) The SAR image was recorded at 17:44:29. The incidence angle at the ship track was 47.6°. The appropriate Bragg wavelength at L-Band (1.24 GHz) is 16.5 cm, and at X-Band (9.35 GHz) is 2.2 cm.

Attributes leading to the selection of JOWIP 1-1 were:

- a. Relatively low uncertainties in crucial parameters such as the pattern propagation speed and ship track location;
- b. Availability of a nearly contemporaneous SAR image;
- c. Availability of good slope gauge data throughout the run;
- d. Availability of video and real aperture radar data in some portion of the run;
- e. Simplicity of the geometry: the near alignment (or counteralignment) of wind, internal wave and ship direction;
- f. A distinctive internal wave signal, covering a range of magnitudes (unlike the case of JOWIP 12-3/4, where internal waves of exceptionally large amplitude were present).

This is also the run in which all participating agencies have expended substantial efforts into

data reduction.

The major drawback of JOWIP 1-1 is that only a short portion of real aperture radar and video camera data exist, and they are non overlapping.

i) Calculated Bragg wave modulation.

Both the 16 and 64 mode smoothed current profiles shown in Figure 2a were used to calculate the spectral modulation for waves which are Bragg resonant with the ERIM SAR at L - and X -bands at the look angle 47.6° . It was noticed that magnitude and phase differed significantly in the calculated results - the 16 mode profile generally yielding a smaller perturbation. In this paper, all calculated results shown were obtained using the 64 mode current profile.

The calculated results at $k_B = 38.36 \text{ m}^{-1}$ (L -band) and $k_B = 289.22 \text{ m}^{-1}$ (X -band) are compared in Figure 3. It is clear that the predicted X -band modulation is significantly smaller than the predicted L -band modulation: the range of variation in f (i.e., $f_{\max} - f_{\min}$) for L -band is 3.4 times larger than for X -band.

To better quantify the comparison, we define the averaged squared modulation density $D(X; X_0)$ as

$$(13) \quad D(X; X_0) = \frac{1}{|X - X_0|} \int_{X_0}^X f^2(x) dx.$$

$D(X; X_0)$ is a measure of the available signal averaged over the interval extending from $x = X_0$ to $x = X$ and gives a measure of the potential detectability of the signal within the interval. In these terms, the potential detectability for the current record extending from $x = 20 \text{ m}$ to $x = 500 \text{ m}$ at L -band is some 23 times larger than at X -band (cf. Figure 4). (Note that the main current structure is confined between $x = 20$ and $x = 400$.)

ii) Comparison with ERIM SAR Cut.

Comparison between these calculations and the ERIM SAR cuts are shown in Figures 5 and 6 for L - and X -bands, respectively. What is compared here is the Bragg model prediction $F(k, x)/F_{eq}(k)$ with the observed ratio $\hat{\sigma}(k, x)/\hat{\sigma}_{bg}(k)$, where $\hat{\sigma}_{bg}$ is the background signal as approximated by the mean level in the interval.

The L -band comparison shows that the calculated modulations, as given by the range of variation in f , are larger by 27% than the modulations in the ERIM SAR cut. The calculated X -band results, however, underpredict the SAR cut by a factor of almost 3.

The detectability measure D defined in Equation (13) can be applied to the case of cross section data by replacing f in its integrand with the relative change $\delta\hat{\sigma}/\hat{\sigma}_{1g}$. The comparison in terms of D for the overlapping interval from $z = 120$ m to $z = 500$ m is displayed in Figure 7. The overall SAR realized detectability is seen to be comparable for L - and X -band, while the detectability predicted by the Bragg model is over 20 times larger for L - than for X -band.

From these comparisons, one is drawn to the conclusion that the model appears to perform reasonably well in predicting the amplitude of the L -band SAR signal, and to underpredict the corresponding X -band SAR result by a factor of order 10. (See Table I)

What is calculated here is the maximum signal available in the context of Bragg scattering to an idealized detector with no loss. A more meaningful comparison, for the purpose of validating the model, is to compare the results to surface slope modulation data and real aperture radar data.

iii) Comparison with Band-Passed Slope Gauge Data.

The modulation of slope in the Bragg resonant component of the surface wave was obtained by band-pass filtering the slope gauge data at the appropriate time-dependent frequency. This time dependence arises from the need to account for the Doppler shift induced by the current as seen by the ship-mounted slope gauge. This is equivalent to a wavenumber filter over a range $[k_B - \Delta k_-, k_B + \Delta k_+]$ centered at the Bragg wavenumber k_B , where Δk_{\pm} is about 15% of k_B . In the calculations, we ignore this finite bandwidth and assume a perfect filter, comparing the calculated $f(k_B)$ with the band-passed slope results for L - and X -band Bragg-wave modulations (see Kwok *et al*, this issue).

In preparation for comparison with calculated results, a 21-point running average (6.3 sec) was performed on the raw data, as shown in Figure 8. This process reduces the total dynamic range of the data by about 5 dB in this case. Comparison between the calculated results and the band-passed slope data is summarized in Table II and displayed in Figures 9 and 10 for L -band and X -band, respectively.

It can be seen that for L -band, the magnitude of the calculated result is in good agreement with the filtered slope data record. The phase of the modulations is not in total agreement. This may be due to the inherent uncertainties associated with phase speed estimates, unsteadiness of the internal wave features, and relative location of the current and slope gauge sensors. The agreement should be considered acceptable.

The X -band comparison shows that the calculations underpredict the magnitude of the modulation. The underprediction (4 db predicted dynamic range vs 25 db observed), is much more

serious than that observed when the calculations were compared with the ERIM SAR cut (4 dB predicted vs 8 dB observed). In terms of the detectability measure, the calculated and experimental $D(500;20)$ are very close for L -band. For X -band, $D(500;20)$ based on the slope gauge measurements is almost 24 times larger than the value based on the calculated f .

The different degree of agreement between the calculations and the data (actually, the difference between the slope gauge and SAR measurements, cf. Figure 11) is consistent with the interpretation that the band-passed slope data represents the total available hydrodynamic signal under the Bragg assumption, and can be achieved only with an ideal detector/processor system. It also indicates that the model is not adequate for X -band.

iv) Comparison with APL Video Data.

The APL video data exists for a short range of JOWIP 1-1 and is compared with the calculated results in Figure 12 for the L -band case. It can be seen that the comparison is good, once again confirming that at least for JOWIP 1-1, the L -band results are well predicted by the calculations.

v) Comparison with TRW X -Band Real Aperture Radar Data.

The TRW X -band real aperture radar operates at 9.13 GHz. During JOWIP 1-1, it was mounted in such a way that the incidence angle was 40° . Data does not exist over the entire range of JOWIP 1-1, but covers a time period starting slightly before the initiation of the run and ending before the large event in the record.

Comparison with the ERIM SAR cut (Figure 13) indicates that the X -band real aperture radar has a much stronger dynamic variation than the ERIM X -band SAR cut (in the overlapping region (from $x = 120$ m to $x = 280$ m), again supporting the contention that there may be more signal available than that detected by the SAR.

The model is found to underpredict the RAR measurements by a factor of almost 10 in the maximum modulation strength found in the range $x = 20$ m to $x = 280$ m: total predicted modulation of 35% to total measured modulation of about 270% (cf. Figure 14 and Table III).

The data displayed in Figure 15 clearly establish a one-to-one relationship between real aperture radar backscatter and band-passed slope power. In particular, the values for $D(280;20)$ differ by less than 15%. The excellent agreement (observed also in all of the other runs) validates the band-pass process. Thus, even though the real aperture radar data is lacking over a significant range making direct quantitative comparison with calculations difficult, conclusions on real aperture radar backscatter modulation are well supported by comparison using the band-passed slope data in this case.

vi) Summary for JOWIP 1-1.

Calculated modulations of the Bragg resonant component using TRW-HIC with the Snyder *et al* (1981) relaxation rate have been compared with experimental data. For *L*-band radar, the model appears successful in predicting the measured modulations, with perhaps a slight underprediction. For *X*-band radar, the model seriously underpredicts the measurements.

The *X*-band underprediction appears less severe in comparisons with ERIM SAR cuts than in comparisons with band-passed slope data and real aperture microwave data. Part of this may be caused by the fact that the band-passed slope data represents the maximum available modulation due to Bragg backscatter, and should only be achieved by an ideal detector/processor. Since the model calculates the maximum available signal, the calculated results are more appropriately compared with the band-passed slope data, as the loss in converting hydrodynamic signature to SAR processed output is not included in the model used.

b. TRW RUN 81B.

This run corresponds to data taken in the time interval from 16:28:40 to 16:38:58 PDT on August 4, 1983. The recorded wind speed at 10 m height was 2.74 m/s blowing towards 123°T. The ship was heading 311°T at an approximately constant speed of 1.2 m/s. The internal waves which induced the current pattern were not steady, their propagation speed ranging from about 0.2 m/s to about 0.5 m/s, with an average speed of 0.27 m/s in an average direction 128°T.

A reason for choosing this run for detailed comparison is that, although no concurrent SAR data is available, the TRW *X*-band real aperture radar data is complete.

The current profile used in the calculation and the wave trajectories of interest are shown in Figure 16.

i) Comparison with Band-Passed Slope Gauge Data.

The band-passed slope data for *L*- and *X*-bands is displayed in Figure 17. It can be seen that the modulation magnitude is comparable for the two cases. In fact, the *X*-band modulation seems to be slightly stronger.

The comparison between the *L*-band calculated result and data is shown in Figure 18. The agreement is very good, even though there is a moderate underprediction of the magnitude of the

modulation. The corresponding comparison for the *X*-band case (Figure 19) shows that the calculation grossly underpredicts the modulation by more than one order of magnitude. Table IV summarizes the relevant information.

ii) Comparison with *X*-Band Real Aperture Radar Data.

Figure 20 compares the band-passed slope data with the *HH* real aperture radar return. In this case, the dynamic range of the modulation in the radar return is somewhat greater than that in the slope data. Calculated modulation and radar data are compared in Figure 21 and Table IV. Calculation again underpredicts data by more than one order of magnitude.

iii) Summary of TRW RUN 81B.

The analysis for this run supports the general conclusions reached for JOWIP 1-1: the model appears acceptable at *L*-band, but it grossly underpredicts the hydrodynamic and radar cross section modulations at *X*-band.

4. EFFECT OF LONG WAVE FIELD.

The wavelength of the Bragg resonant surface wave component is about 2 cm for *X*-band and 17 cm for *L*-band. One of the reasons proposed for explaining the poor performance of the model at *X*-band is that these short Bragg resonant components are strongly affected by longer surface waves.

A. Formulation.

Alpers, Ross and Rufenach (1981) considered three mechanisms by which a deterministic long wave field can affect the statistical properties of short Bragg waves as they are viewed by SAR. These are, the *tilt* mechanism, in which the long waves alter the local angle of incidence of the radar; the *hydrodynamic* mechanism, in which short wave density is modulated by the straining action of the long waves (based on the radiation stress mechanism); and the *velocity bunching* mechanism, in which the synthesized radar intensity is modulated due to phase modulation in the Doppler return induced by long wave orbital velocity. The hydrodynamic mechanism affects the spectral content of the surface waves; the tilt mechanism affects radar backscatter return; and the velocity bunching mechanism affects only SAR return.

Alpers *et al* showed that in the presence of a deterministic long wave field described by the Fourier spectrum $Z(\vec{k})$, where \vec{k} is the long wave wave-vector, the backscatter due to Bragg scattering can be expressed as:

$$(14) \quad \sigma = \langle \sigma \rangle \left[1 + \int_0^{K_R} \mathcal{M} d\vec{k} \right],$$

where $\langle \sigma \rangle$ is the radar backscatter cross section when the long wave field is absent or averaged out. The integrand is defined by

$$(15) \quad \mathcal{M} = R(\vec{k}) Z(\vec{k}) e^{i\vec{k} \cdot \vec{r} - i\Omega t} + c.c.$$

where $\Omega(\vec{k})$ is the long wave frequency, $Z(\vec{k})$ is related to the surface elevation $\eta_L(\vec{x}, t)$ of the long waves through

$$(16) \quad \eta_L(\vec{x}, t) = \int Z(\vec{k}) e^{i\vec{k} \cdot \vec{x} - i\Omega t} d\vec{k} + c.c.,$$

and $R(\vec{k})$ is a complex modulational transfer function (MTF) associated with the long wave field effect.

The MTF $R(\vec{k})$ is composed of three terms according to the three mechanisms described above:

$$(17) \quad R = R^{TILT} + R^{HYDRO} + R^{VB}.$$

Detailed expressions for R can be found in Alpers *et al* (1981) or Vesecky and Stewart (1982).

In the present application, all of the waves which may have an effect on the short Bragg waves are considered. We identify $\langle \sigma \rangle$ with the Bragg theory cross section σ_B in the absence of long waves,

and combine Equations (14) through (17) to obtain

$$(18) \quad \sigma = \sigma_B (1 + I_1 + I_2 + I_3)$$

$$= \sigma_B \left[1 + \int_0^{K_U} \mathcal{M}(\vec{k}) d\vec{k} + \int_{K_U}^{K_R} \mathcal{M}(\vec{k}) d\vec{k} + \int_{K_R}^{K_C} \mathcal{M}(\vec{k}) d\vec{k} \right].$$

In Equation (18), I_1 represents the contribution from waves long compared with the current pattern of interest, I_2 represents the contribution from waves longer than the resolution cell width but shorter than the scale of the current pattern, and I_3 represents the contribution from waves longer than the "dividing wavelength" (empirically defined as γ times the Bragg wavelength, where γ is order 1, usually taken to be between 2 and 6), but shorter than the resolution cell width. A schematic sketch is shown in Figure 22.

The long wave field is taken to be random and described statistically. The RMS of σ taken over spatial scales large compared with the resolution cell width can be written as:

$$(19) \quad \sqrt{\overline{\sigma\sigma^*}} = \sigma_B \left[\overline{(1 + I_1)^2} + \overline{I_2^2} + \overline{I_3^2} \right]^{1/2}.$$

Terms linear in I_1 survive the averaging process, but terms linear in I_2 or I_3 average out to zero. The long wave field effects are represented by $\overline{I_2^2}$ and $\overline{I_3^2}$.

In order to compute the right hand side of Equation (10), we assume that η_L is a stationary random process. The one-time, two-point correlation function $\rho(\vec{\xi}, t)$ is defined as

$$(20) \quad \rho(\vec{\xi}, t) = \overline{\eta_L(\vec{x}, t) \eta_L(\vec{x} + \vec{\xi}, t)}$$

where the overbar now denotes ensemble average. The long wave power spectrum $\Psi_L(\vec{k})$ is just the Fourier transform of $\rho(\vec{\xi})$:

$$(21) \quad \Psi_L(\vec{k}) = \int \rho(\vec{\xi}) e^{i\vec{k} \cdot \vec{\xi}} d\vec{\xi},$$

and it follows that

$$(22) \quad \overline{Z(\vec{k}) Z^*(\vec{k}_1)} = \Psi_L(\vec{k}) \delta(\vec{k} - \vec{k}_1).$$

The ensemble averaging can now be identified with spatial averaging over scales long compared with the resolution cell width (and the Bragg wavelength), but short compared with the spatial scales of the surface current pattern associated with subsurface disturbances. As mentioned earlier, this averaging process leaves I_1 unaltered, but averages out the linear contributions of I_2 and I_3 .

From the definition of I_2 and I_3 , we obtain

$$(23) \quad \begin{aligned} \overline{I_2^2} &= \int_{K_U}^{K_R} d\vec{k} \int_{K_U}^{K_R} d\vec{k}_1 \overline{\mathcal{A}(\vec{k}) \mathcal{A}^*(\vec{k}_1)} \\ &= \int_{K_U}^{K_R} |R(\vec{k})|^2 \Psi_L(\vec{k}, \vec{x}) d\vec{k} \end{aligned}$$

where the dependence on \vec{x} is made explicit to emphasize the fact that the long wave field is varying on a scale large compared with the averaging dimensions. In this way, the modulation due to the current pattern is preserved. Similarly, $\overline{I_3^2}$ is obtained as:

$$(24) \quad \overline{I_3^2} = \int_{K_R}^{K_C} |R(\vec{k})|^2 \Psi_L(\vec{k}, \vec{x}) d\vec{k}.$$

The modulated RMS radar cross section that corresponds to Bragg backscattering with long wave field effects included is therefore

$$(25) \quad \sigma_{RMS} = \sqrt{\sigma^2} = \sigma_B(\vec{k}_B; \vec{x}) \left[(1 + I_1)^2 + \int_{K_U}^{K_C} |R(\vec{k})|^2 \Psi_L(\vec{k}, \vec{x}) dK \right]^{1/2},$$

with I_1 given by

$$(26) \quad I_1 = \int_0^{K_U} \mathcal{A}(\vec{k}) d\vec{k}.$$

In Equation (25) the term involving the integral represents contributions from long waves which are longer than the dividing wavelength, but shorter than the current pattern. The terms involving I_1 , on the other hand, represents contributions from waves comparable to or longer than the current pattern. This is a clutter term, since it produces modulations with spatial scales similar to that of the signal obtained from the varying current.

B. Application to Present Calculations.

When the long wave field effect is included, the backscatter cross section in the absence of a current becomes (in the unidirectional formulation)

$$(27) \quad \sigma_{eq} = \sigma_0(k_B) [1 + \mathcal{L}_0(k_B)],$$

where $\sigma_0(k_B)$ has been defined in Equation (2) and $\mathcal{L}_0(k_B)$ is the long wave field effect on the Bragg wave component in the equilibrium state (i.e., independent of x). In the presence of a current, the long wave field effect \mathcal{L} is dependent on x and is given by

$$(28) \quad \mathcal{L}(k, x) = \int_0^{K_C} |R(k, K)|^2 \Psi_L(K, x) dK,$$

where $\Psi_L(K, x)$ is the long wave spectrum perturbed by the current. The maximum potential relative change in radar cross section becomes

$$(29) \quad \frac{\delta \sigma}{\sigma_{eq}} = \left(1 + f(k_B, x) \right) \left[\frac{1 + \mathcal{L}(k_B, x)}{1 + \mathcal{L}_0(k_B)} \right]^{1/2} - 1.$$

Comparison between predictions by the Bragg model and predictions by the model including long wave effects involves the comparison of $f(k_B, x)$ with the right hand side of Equation (29), which we denote as the dimensionless modulation $m(k, x)$.

In the cases exhibited, the look direction and wind direction are generally aligned, so that the velocity bunching mechanism can be neglected. When comparing with band-passed slope gauge data, only the hydrodynamic term (R^{HYDRO}) in Equation (17) is operative. When comparing with real aperture radar data, both the hydrodynamic and tilt (R^{TILT}) terms are included.

C. Results of Calculation with Long Wave Field Effects.

The comparison between relative cross section variations predicted by Bragg theory with and without long wave effects for JOWIP 1-1 is shown in Figures 23 and 24 for L - and X -bands respectively. The long wave field effect increases the potential detectability $D(500;20)$ by less than 10% at L -band, whereas the increase is almost 300% at X -band (cf. Table V).

This effect is also observed in the case of TRW RUN 81B. The comparison of results with and

without long wave field effects for L - and X -bands is shown in Figures 25 and 26 respectively. In this case, $X_0 = -729$ m and $X = -9$ m. The enhancement at L -band, as given by the detectability measure, is less than 5%, but the enhancement at X -band is almost 200%. Long wave field effects on the predicted modulations are summarized in Table VI.

Part of the reason that the long wave field effect is stronger at X -band than at L -band is that more waves qualify as "long waves" affecting the short X -band Bragg waves. Another reason is that the "long waves" included in the X -band case are strongly modulated.

It should be pointed out that since the long wave field effect depends on the shape of the surface wave spectrum, it is also a function of wind speed. This dependence on wind speed is complicated. On the one hand, an increase in wind speed shifts the spectrum to longer waves and make more "long waves" available. On the other hand, an increase in wind speed weakens the modulation of all waves. Thus, for a given current pattern, there should be a wind speed for which the signal is maximum.

Figure 27a compares the calculated X -band results (with long wave field effects) to X -band slope data for JOWIP 1-1. The discrepancy is reduced but there is still an underprediction: the $D(500;20)$ value based on the calculation underpredicts the actual detectability found in the slope gauge signal by a factor of 6 (cf. Figure 27b).

The comparison with the ERIM SAR data is displayed in Figure 28, which shows a theoretical underprediction, based on $D(500;120)$, by a factor of 1.6.

The corresponding comparisons for TRW 81B are shown in Figure 29 (against band-passed slope data) and Figure 30 (against real aperture radar). Based on $D(-729,-9)$, the calculation including hydrodynamic long wave effects underpredicts the slope gauge data by about a factor of 50, down from around 93 predicted by the Bragg model. The calculation including both hydrodynamic and tilt mechanism underpredicts the detectability of the RAR data in the same range by a factor of 53 (VV data) and a factor of 49 (HH data). The underpredictions without long wave effects were by factors of 107 and 138, respectively.

In summary, long wave field effects do not alter the relatively good agreement at L -band, but significantly reduce the discrepancy at X -band. However, even with the long wave field effects included, the underprediction at X -band is not eliminated.

5. SUMMARY AND CONCLUSIONS

Model calculations of surface wave modulation by surface currents have been compared with field measurements made with SAR (X - and L -bands), real aperture radar (X -band), slope gauge (band-passed at X - and L -band Bragg wave frequencies), and to a limited extent, CCD video camera (processed for L -band Bragg wave wavenumber). The following observations have been made:

1. Among several wind-relaxation models used in the calculation, the model proposed by Snyder *et al* (1981) yields the best agreement with data. The Inoue (1966) model, used extensively in the past, yields modulations an order of magnitude smaller and should be rejected.

2. A theoretical model based on simple Bragg scattering and wind-relaxation predicts modulations measurable at X -band to be an order of magnitude or more smaller than those measurable at L -band. This is in disagreement with the observations (including SAR, RAR and slope gauge data) which show that the modulation magnitudes at X - and L -bands are similar.

3. The model calculations for L -band modulations show reasonable agreement with measurements. Specifically, the calculations agree well with slope gauge data and CCD video camera data, and slightly overpredict the SAR modulations.

4. The model calculations for X -band modulations underpredict the measurements. Based on a measure of overall detectability, the underprediction is by about a factor of 10 when compared with SAR, and by a factor of 20 to 40 when compared with real aperture radar and slope gauge data smoothed to approximate a spatial resolution comparable to that of the SAR.

5. A new model which incorporates the effects of modulated long surface waves on Bragg waves shows that the long wave field (LWF) effect enhances the theoretical results by only a few percent at L -band, but by 100% to 300% at X -band. Therefore, the LWF effect, when included, reduces the discrepancy between model and data at X -band without affecting the generally good agreement at L -band.

6. Even with the LWF effects included, the model underpredicts X -band modulation by a factor of 3 when compared with SAR, and a factor of 10 to 30 when compared with real aperture radar and slope gauge data.

It should be emphasized that the above observations are based on a limited set of data and comparisons. Further analysis of data for cases with weaker surface currents and a wider range of

surface conditions is underway and will be reported subsequently.

Acknowledgements

The current meter and raw slope gauge data were obtained from B. A. Hughes and S. J. Hughes of the Defense Research Establishment Pacific, Canada. The SAR data were obtained from R. A. Shuchman and D. R. Lyzenga of the Environmental Research Institute of Michigan. The CCD video camera data were obtained from B. Gotwols from the Applied Physics Laboratory of The Johns Hopkins University. The real aperture radar and the band-passed slope data were obtained from D. Kwoh of the Fluid Mechanics Department of TRW. We also thank A. Bruckheim, the DARPA program manager; B. Lake of TRW who managed the TRW team; T. Taylor and R. Gasparovic for numerous interesting discussions, and D. Thompson of the Applied Physics Laboratory for forwarding us a tape of the current meter data.

REFERENCES.

- Alpers, W., and Hennings, I.: A Theory of the Imaging Mechanism of Underwater Bottom Topography by Real and Synthetic Aperture Radar, *J. Geophys. Res.* 89, 10529-10546, 1984.
- Alpers, W.R., Ross, D.B., and Rufenach, C.L.: On the Detectability of Ocean Surface Waves by Real and Synthetic Aperture Radar, *J. Geophys. Res.* 86, 6481-6498, 1981.
- Holliday, D., St-Cyr, G., and Woods, N.E.: A radar ocean imaging model for small to moderate incidence angles, *Int. J. Remote Sensing* 7, 1809-1834, 1986.
- Hughes, B.A.: The Effect of Internal Waves on Surface Wind Waves: Part 2, Theoretical Analysis, *J. Geophys. Res.* 83, 455-465, 1978.
- Inoue, T.: On the Growth of the Spectrum of a Wind Generated Sea According to a Modified Miles-Phillips Mechanism and its Application to Wave Forecasting, *New York Univ. Geophys. Sci. Lab. Rep. TR67-5*, 1966.
- Kwoh, D.S.W., Lake, B.M. and Rungaldier, H.: A Shipboard Real Aperture Radar Measurement in JOWIP (The Georgia Strait Experiment), *J. Geophys. Res.*, this issue.
- Miles, J.W.: On the Generation of Surface Waves by Shear Flows, Part 2, *J. Fluid Mech.* 6, 568-582, 1959.
- Mitsuyasu, H., and Honda, T.: Wind-induced Growth of Water Waves, *J. Fluid Mech.* 123, 425-442, 1982.
- Pierson, W.J., and Stacy, R.A.: The Elevation, Slope and Curvature Spectra of a Wind Roughened Sea Surface, *NASA CR-2247*, 1973.
- Plant, W.J.: A Relationship between Wind Stress and Wave Slope, *J. Geophys. Res.* 87, 1961-1967, 1982.
- Snyder, R.L., and Cox, C.S.: A Field Study of the Wind Generation of Ocean Waves, *J. Mar. Res.* 24, 141-178, 1966.
- Snyder, R.L., Dobson, F.W., Elliott, J.A., and Long, R.B.: Array Measurements of Atmospheric Pressure Fluctuations above Surface Gravity Waves, *J. Fluid Mech.* 102, 1-59, 1981.
- Vesecky, J., and Stewart, R.: The Observation of Ocean Surface Phenomena Using Imagery from the SEASAT Synthetic Aperture Radar: An Assessment, *J. Geophys. Res.* 87, 3397-3430, 1982.
- Wright, J.W.: Backscattering from Capillary Waves with Application to Sea Clutter, *IEEE Trans. AP-14*, 749-754, 1966.

TABLE 1: JOWIP 1-1. (z range: 120 m to 500 m)
SAR modulations compared to Bragg theory predictions

	f_{min}	f_{max}	F/F_{eq} dynamic range	Detectab at $z=500$ m
L-band calculated	0.006	2.685	26.9 db	0.391
L-band SAR	0.070	2.168	14.9 db	0.213
X-band calculated	0.531	1.319	4.0 db	0.017
X-band SAR	0.338	2.372	8.5 db	0.152

TABLE II: JOWIP 1-1. (x range: 20 m to 500 m)
Slope Gauge modulations compared to Bragg theory predictions

	f_{min}	f_{max}	F/F_{eq} dynamic range	Detectab at $x=500$ m
L-band calculated	0.006	2.685	26.9 db	0.329
L-band Slope Gauge	0.004	3.813	30.2 db	0.333
X-band calculated	0.530	1.319	4.0 db	0.014
X-band Slope Gauge	0.009	3.235	25.4 db	0.333

TABLE III: JOWIP 1-1. (z range: 20 m to 280 m)
RAR modulations compared to Bragg theory predictions

	f_{min}	f_{max}	F/F_{eq} dynamic range	Detectab at $z=280$ m
X-band calculated	0.854	1.205	1.5 db	0.006
X-band RAR	0.025	2.708	20.3 db	0.267

TABLE IV: TRW 81B. (x range: -729 m to -9 m)
Slope gauge and RAR modulations compared
to Bragg theory predictions.

	f_{min}	f_{max}	F/F_{eq} dynamic range	Detectab at $x = -9$ m
L-band calculated	0.005	1.925	25.7 db	0.264
L-band Slope Gauge	0.001	3.455	35.7 db	0.562

X-band calculated	0.511	1.320	4.1 db	0.010
X-band Slope Gauge	0.338	2.372	21.7 db	0.933
X-band RAR (VV)	0.006	5.311	29.5 db	1.067
X-band RAR (HH)	0.005	6.165	30.5 db	1.378

TABLE V: JOWIP 1-1. (z range: 20 m to 500 m)
Long Wave Field effects on predicted modulations.

L -BAND:	f_{min}	f_{max}	F/F_{eq} dynamic range	Detectab at $z=500$ m
Bragg	0.006	2.685	26.9 db	0.329
+Hydro	0.005	2.616	26.9 db	0.333
+Hydro+Tilt(VV)	0.005	2.600	26.9 db	0.338
+Hydro+Tilt(HH)	0.005	2.563	27.1 db	0.360

X -BAND:				
Bragg	0.530	1.319	4.0 db	0.014
+Hydro	0.446	1.587	5.5 db	0.029
+Hydro+Tilt(VV)	0.436	1.659	5.8 db	0.032
+Hydro+Tilt(HH)	0.386	1.942	7.0 db	0.052

TABLE VI: TRW 81B. (x range: -729 m to -9 m)
Long Wave Field effects on predicted modulations.

L -BAND:	f_{min}	f_{max}	F/F_{eq} dynamic range	Detectab at $x = -9$ m
Bragg	0.005	1.925	25.7 db	0.264
+Hydro	0.005	1.931	25.8 db	0.267
+Hydro+Tilt(VV)	0.005	1.932	25.9 db	0.271
+Hydro+Tilt(HH)	0.005	1.967	26.1 db	0.277

X -BAND:

Bragg	0.511	1.320	4.1 db	0.010
+Hydro	0.441	1.509	5.3 db	0.019
+Hydro+Tilt(VV)	0.435	1.561	5.6 db	0.020
+Hydro+Tilt(HH)	0.402	1.787	6.5 db	0.028

FIGURE CAPTIONS.

- Figure 1. a) Relaxation rate β as a function of wavenumber k in the range containing Bragg resonant waves with L - and X -band radiation. (Wind speed is 5 m/s blowing in the \vec{k} direction).
b) X -band results for the conditions of JOWIP 1-1 using various relaxation rate models.

- Figure 2. JOWIP 1-1:
a) current as a function of distance along the ship's track. Full line: 64 mode FFT smoothing. Dotted line: 16 mode FFT smoothing.
b) Selected one-dimensional ray trajectories in k - z space for the current (64 mode smoothing) displayed in (a). The horizontal lines indicate approximate position of Bragg resonant k values for L - and X -band radiation.

- Figure 3. JOWIP 1-1: Current induced modulation of the relative perturbation spectral density $F(k_B, z)/F_{eq}(k_B) = 1 + f(k_B, z)$ calculated for the 64 mode current of Figure 2.
Full line: L -band resonant wave ($k_B = 38.36 \text{ m}^{-1}$).
Dotted line: X -band resonant wave ($k_B = 289.22 \text{ m}^{-1}$).
a) linear scale,
b) log scale in db.

- Figure 4. Potential detectability [cf. Equation (13)] for the results displayed in Figure 3.

- Figure 5. JOWIP 1-1: L -band. Comparison between calculated Bragg wave modulation $F(k_B, z)/F_{eq}(k_B)$ (dotted line) and relative cross section $\sigma(z)/\sigma_{eq}$ (full line) in the ERIM SAR cut.
a) linear plot,
b) log plot in db.

- Figure 6. JOWIP 1-1: X -band. Comparison between calculated Bragg wave modulation

$F(k_B, x)/F_{eq}(k_B)$ (dotted line) and relative cross section $\sigma(x)/\sigma_B$ (full line) in the ERIM SAR cut.

- a) linear plot,
- b) log plot in db.

Figure 7. JOWIP 1-1: SAR achieved detectability (full line) compared to Bragg model potential detectability (dotted line).

- a) L-band,
- b) X-band.

Figure 8. JOWIP 1-1: Band-passed slope gauge data. Dotted line: raw data. Full line: 21 point average (6.3 sec).

- a) filtered around L-band,
- b) filtered around X-band.

Figure 9. JOWIP 1-1: L-Band. Comparison between slope gauge and calculated Bragg wave modulation. Full line: relative power around $k_B = 38.36 \text{ m}^{-1}$ in units of the average power for the interval. Dotted line: Calculated $F(k_B, x)/F_{eq}(k_B)$

- a) linear plot,
- b) log plot in db.

Figure 10. JOWIP 1-1: X-Band. Same as Figure 9 caption, but $k_B = 289.22 \text{ m}^{-1}$.

Figure 11. JOWIP 1-1: Comparison between normalized slope gauge power (full line) and normalized SAR cross section (dotted line).

- a) L-band,
- b) X-band.

Figure 12. JOWIP 1-1: Normalized spectrum $F(k_B, x)/F_{eq}(k_B)$ at L-band.

Full line: APL video data results,
Dotted line: predicted by Bragg model.

Figure 13. JOWIP 1-1: X-band. Comparison between TRW's RAR (full line) and ERIM's SAR (dotted line) cross sections.

Figure 14. JOWIP 1-1: X-band. Comparison between normalized RAR cross section (full

line) and Bragg model normalized spectral density (dotted line).

- a) linear plot,
- b) log plot in db.

Figure 15. JOWIP 1-1: X-band. Comparison between normalized RAR cross section (full line) and normalized slope gauge power (dotted line).
a) linear plot.
b) log plot in db.

Figure 16. TRW 81B:
a) Surface current profile.
b) Selected ray trajectories in k - z space for the current shown in (a).

Figure 17. TRW 81B: Band passed slope gauge data. Full line: L-band; dotted line: X-band.
a) linear plot,
b) log plot in db.

Figure 18. TRW 81B: L-band. Comparison between band-passed slope gauge data (full line) and Bragg Model Calculation (dotted line).
a) linear plot,
b) log plot in db.

Figure 19. TRW 81B: X-band. Comparison between band-passed slope gauge data (full line) and Bragg Model Calculation (dotted line).
a) linear plot,
b) log plot in db.

Figure 20. TRW 81B: X-band. Comparison between band-passed slope gauge data (full line) and TRW's RAR normalized HH cross section.

Figure 21. TRW 81B: X-band. Comparison between TRW's RAR HH cross section (full line) and Bragg Model Calculation (dotted line).

Figure 22. Schematic representation of long wave contributions to the spectrum modulation at k_B .

- Figure 23. JOWIP 1-1: *L*-band. Comparison between computational results with (full line) and without (dotted line) long wave field effects.
a) predicted relative cross section,
b) predicted potential detectability.
- Figure 24. JOWIP 1-1: *X*-band. Comparison between computational results with (full line) and without (dotted line) long wave field effects.
a) predicted relative cross section,
b) predicted potential detectability.
- Figure 25. TRW 81B: *L*-band. Comparison between computational results with (full line) and without (dotted line) long wave field effects.
a) predicted relative variation in cross section,
b) predicted potential detectability.
- Figure 26. TRW 81B: *X*-band. Comparison between computational results with (full line) and without (dotted line) long wave field effects.
a) predicted relative variation in cross section,
b) predicted potential detectability.
- Figure 27. JOWIP 1-1: *X*-band. Comparison between band-passed slope gauge data (full line) and LWF model calculations (dotted line).
a) normalized power,
b) detectability.
- Figure 28. JOWIP 1-1: *X*-band. Comparison between ERIM's SAR data (full line) and LWF model calculations (dotted line).
a) relative cross section,
b) detectability.
- Figure 29. TRW 81B: *X*-band. Comparison between ERIM's SAR data (full line) and LWF model calculations (dotted line).
a) relative cross section,
b) detectability.
- Figure 30. TRW 81B: *X*-band. Comparison between TRW's *HH* RAR data (full line) and

LWF model calculations (dotted line).

a) relative cross section

b) detectability.

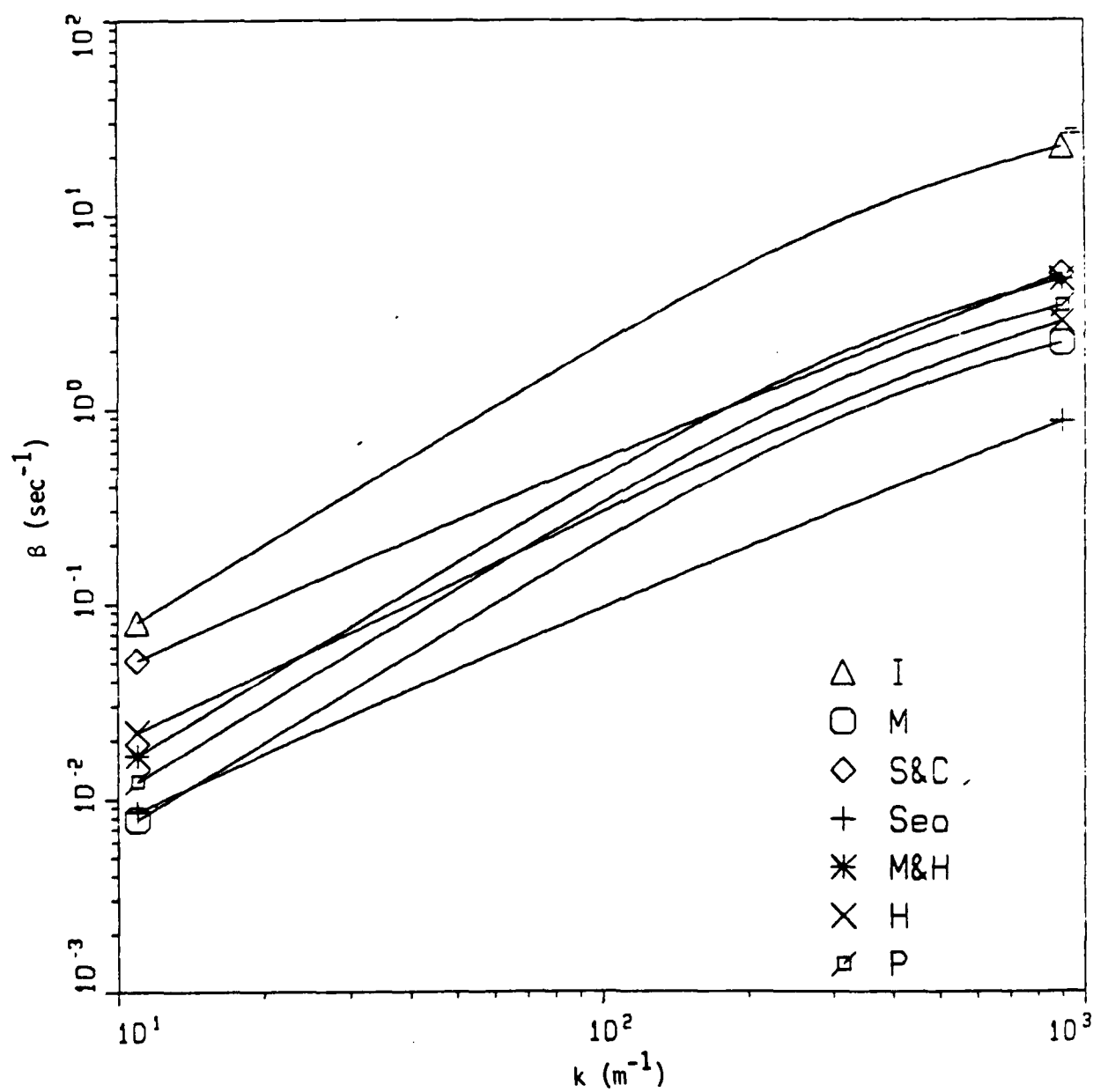


FIGURE 1.a

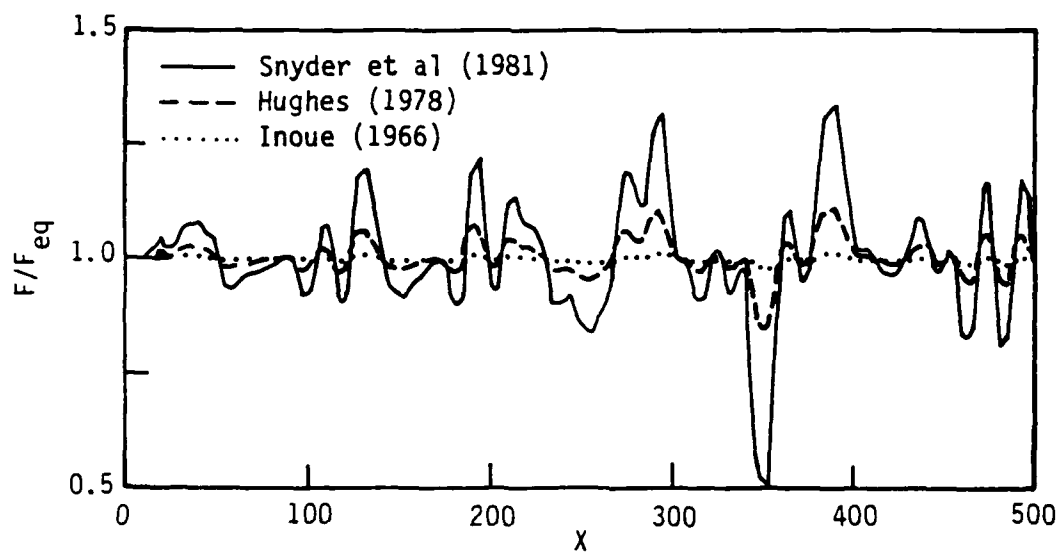


FIGURE 1.b

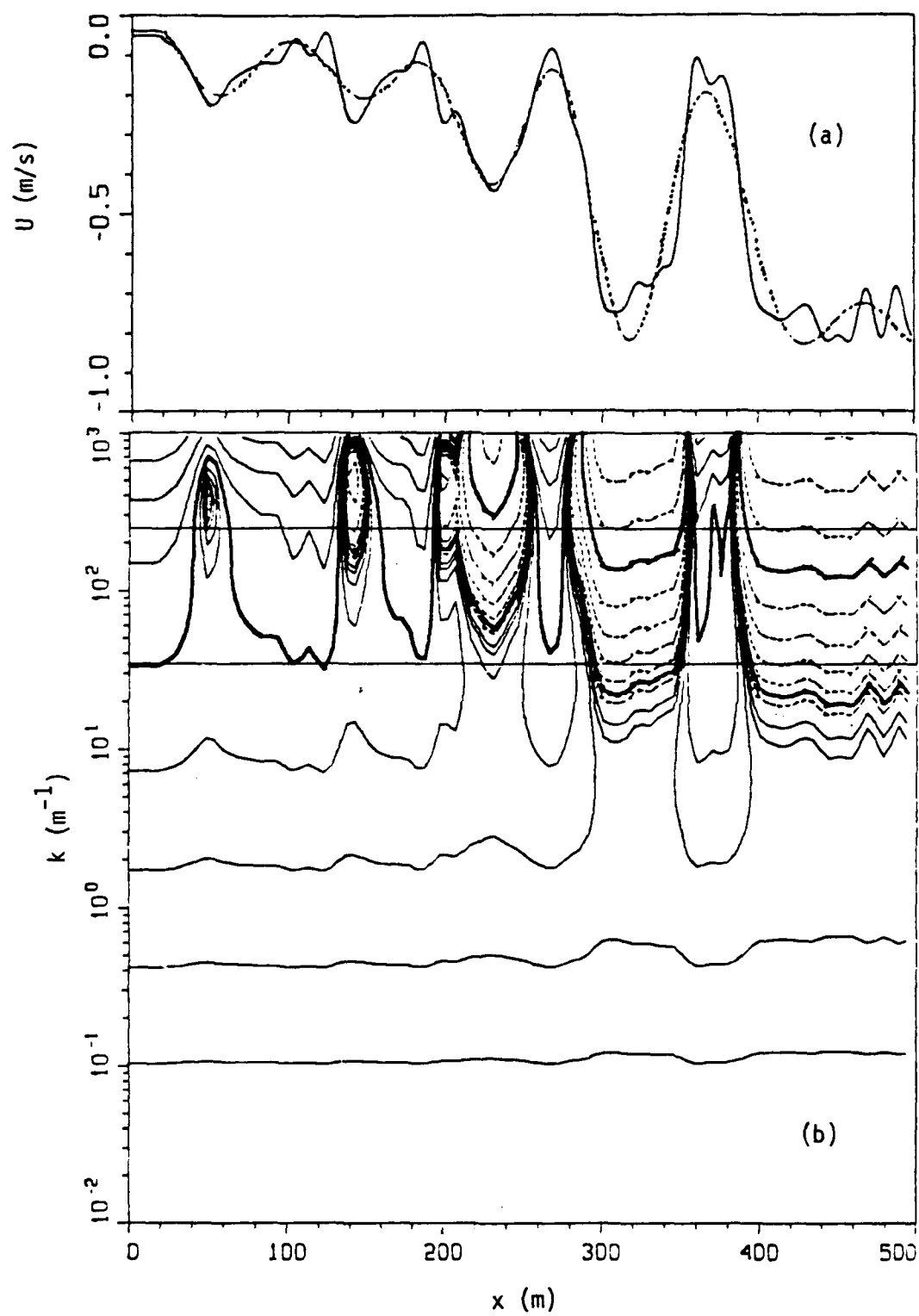


FIGURE 2

BRAGG MODEL

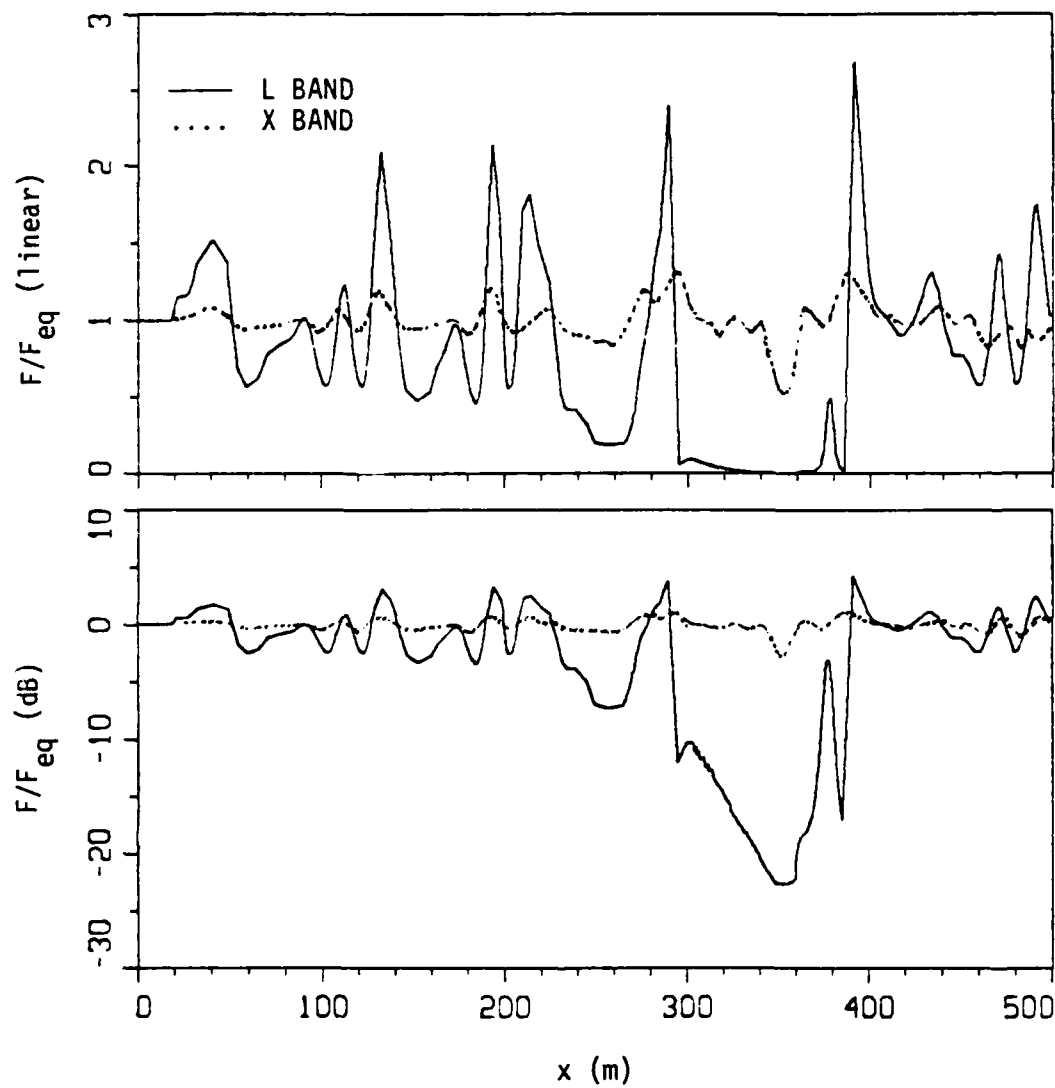


FIGURE 3

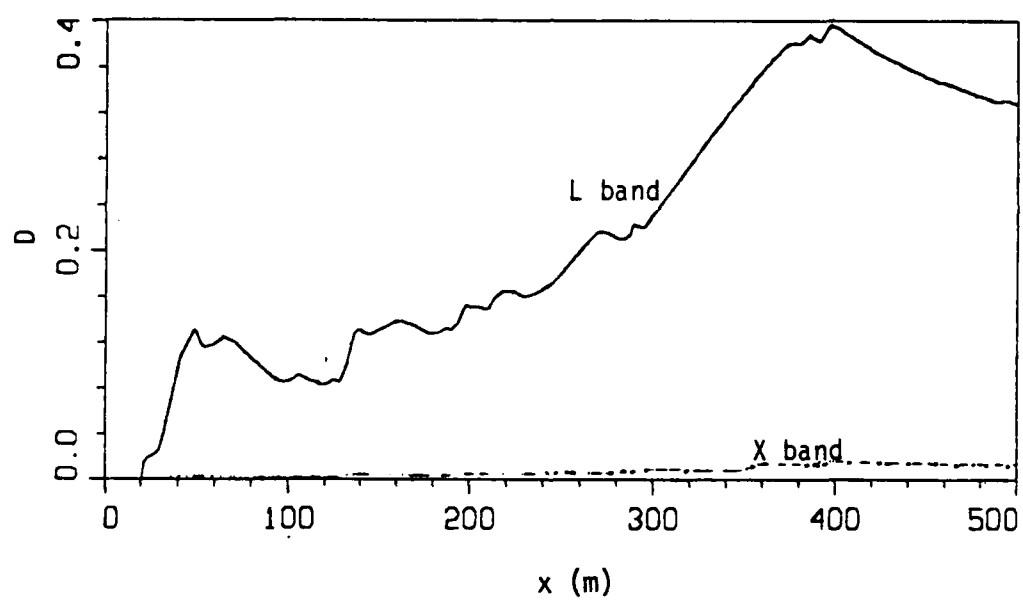


FIGURE 4

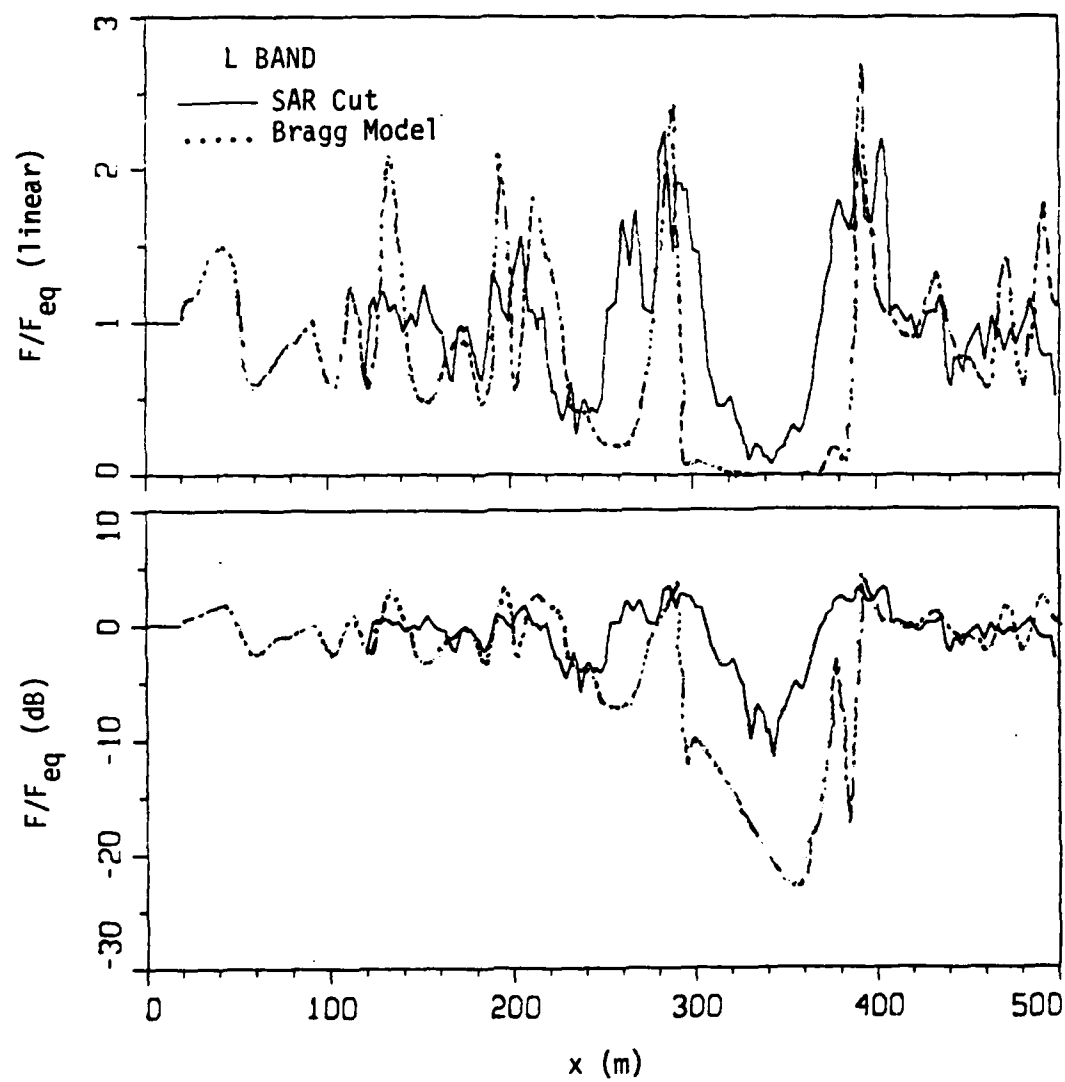


FIGURE 5

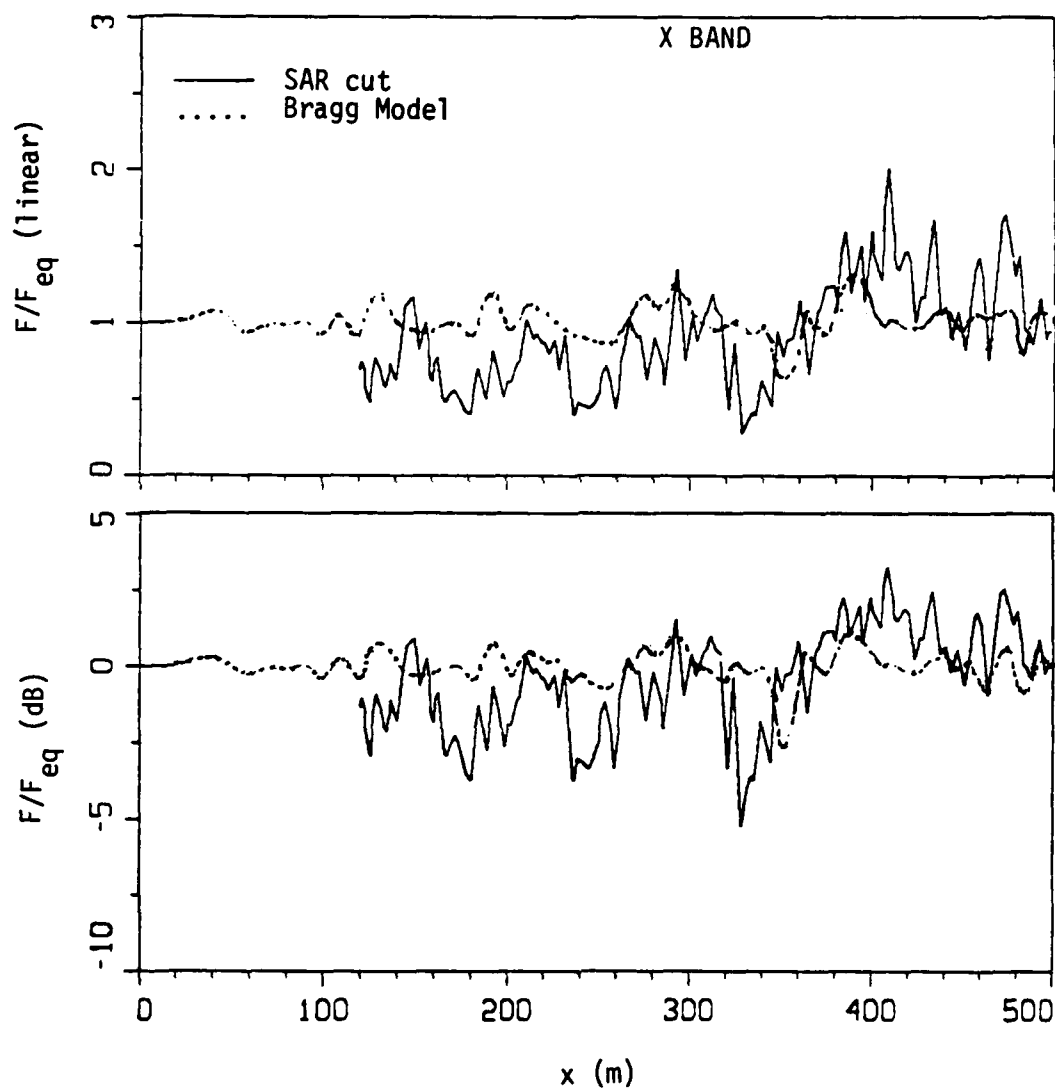


FIGURE 6

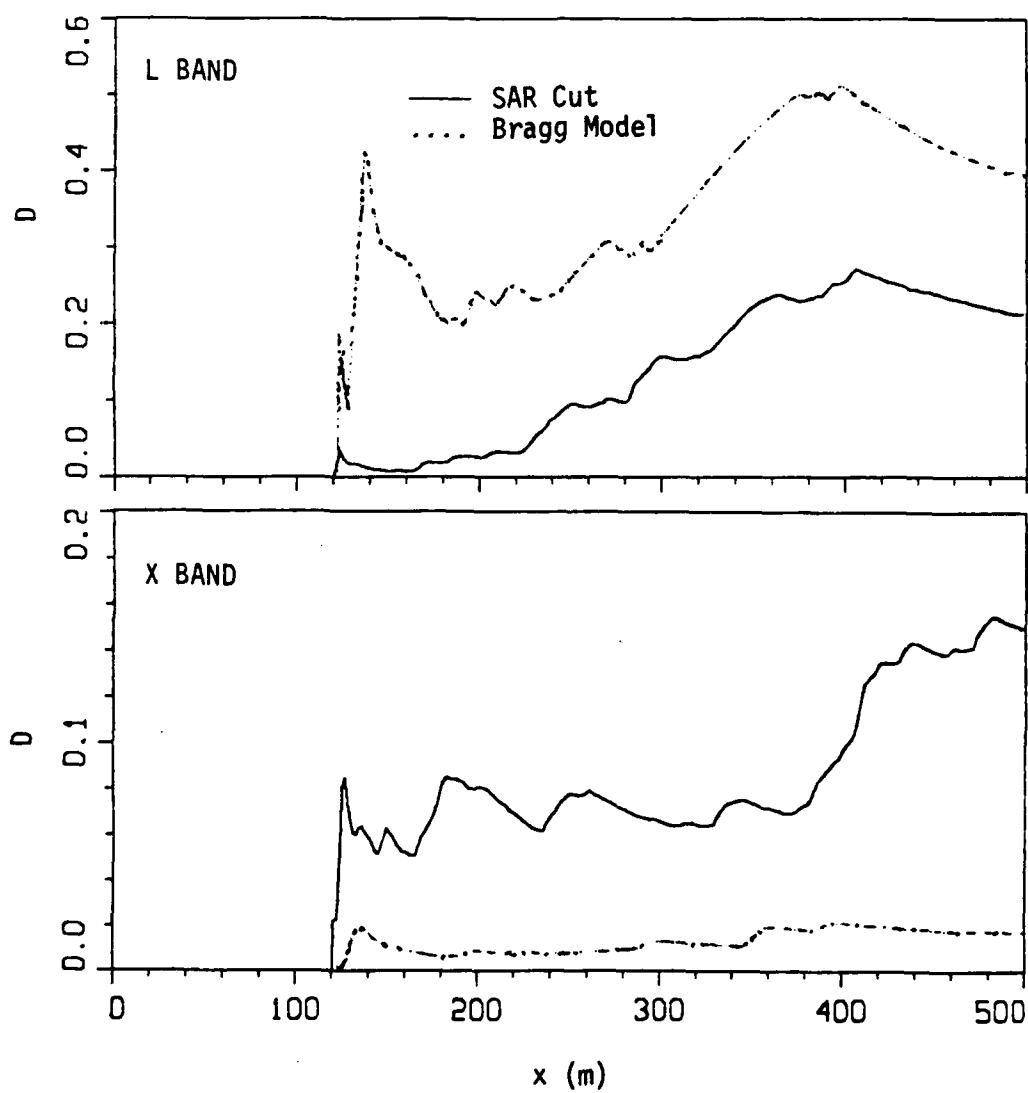


FIGURE 7

BAND-PASSED SLOPE GAUGE DATA
RAW AND AVERAGED (6.3 SEC RUNNING AVERAGE)

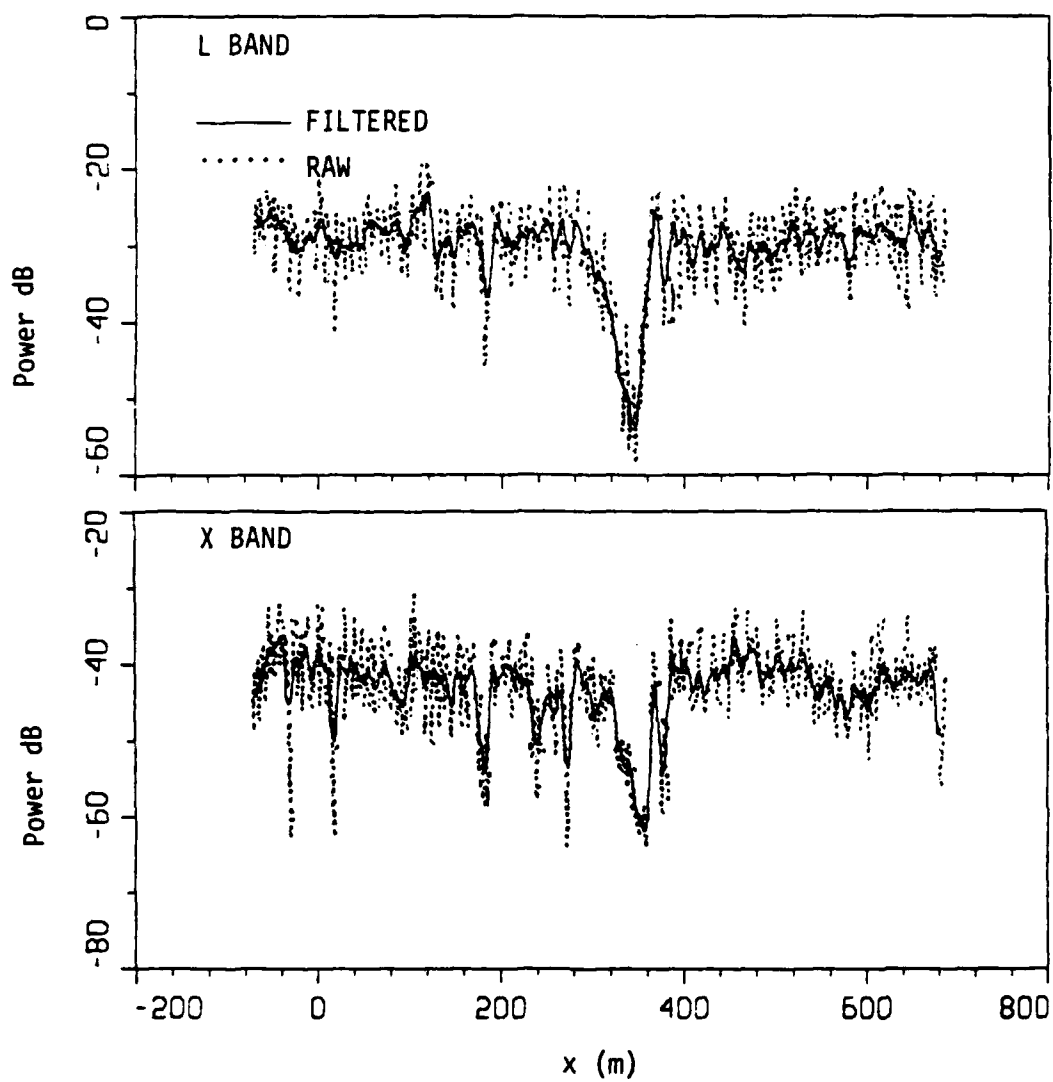


FIGURE 8

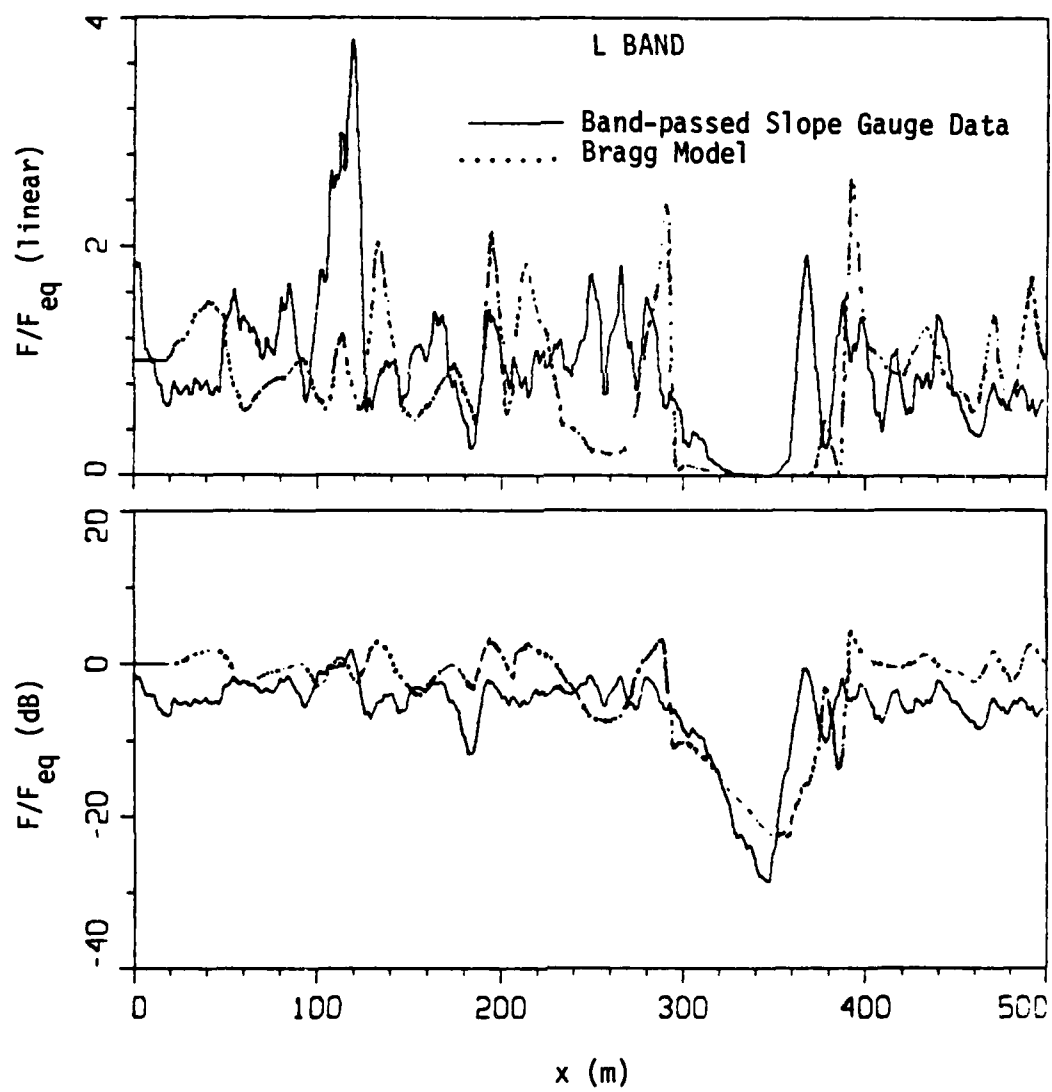


FIGURE 9

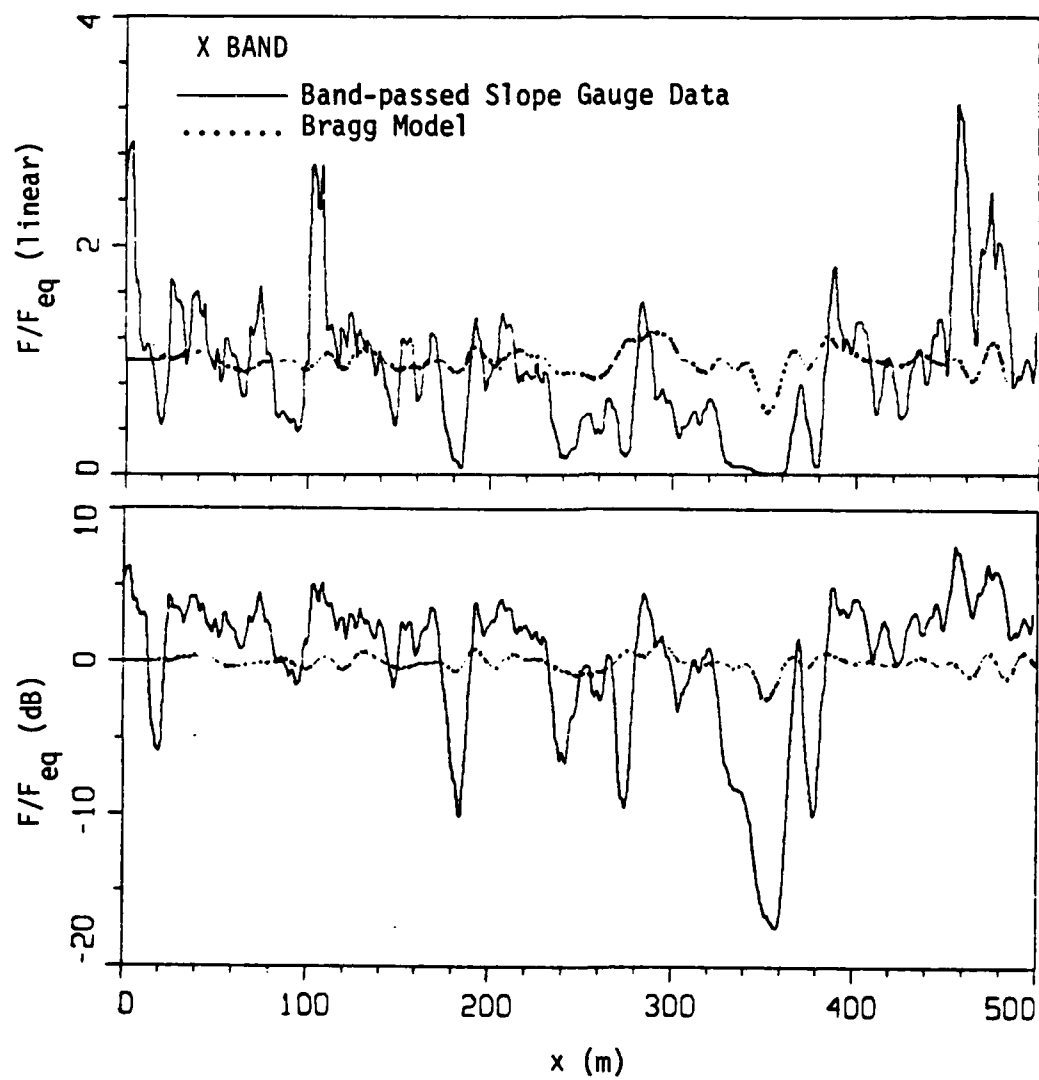


FIGURE 10



FIGURE 11

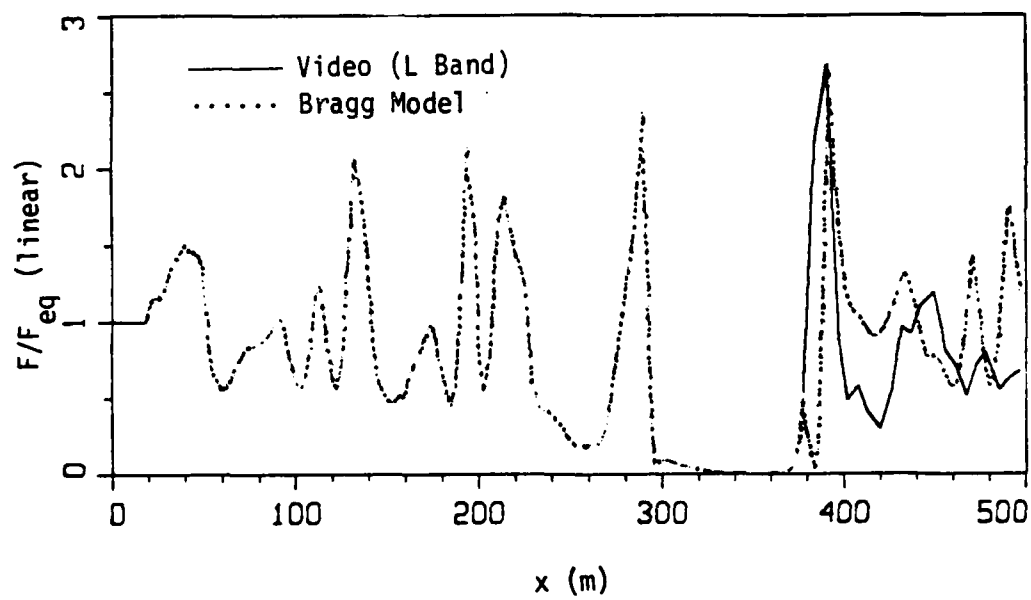


FIGURE 12

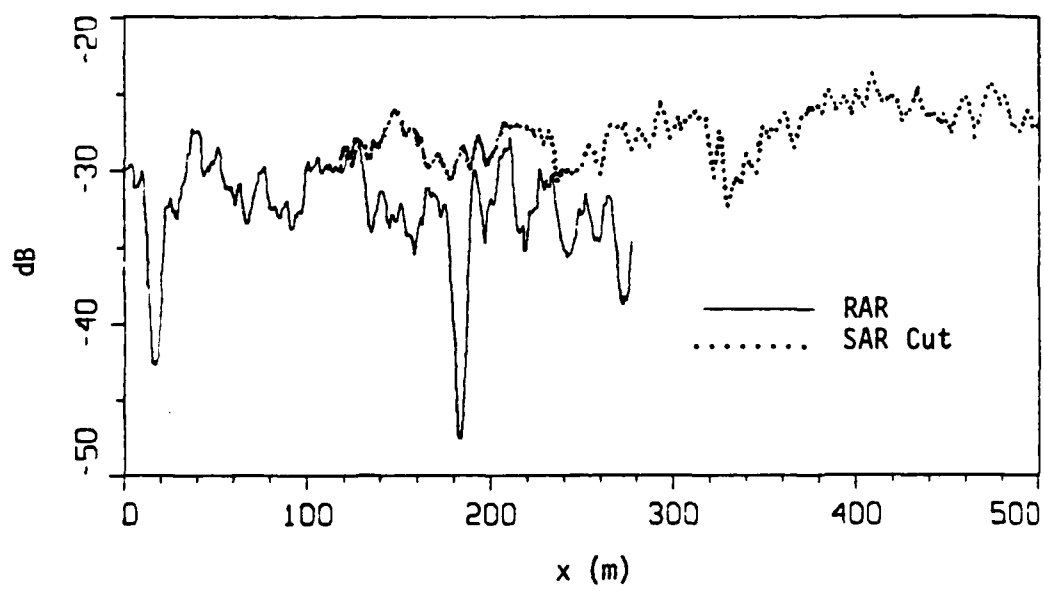


FIGURE 13

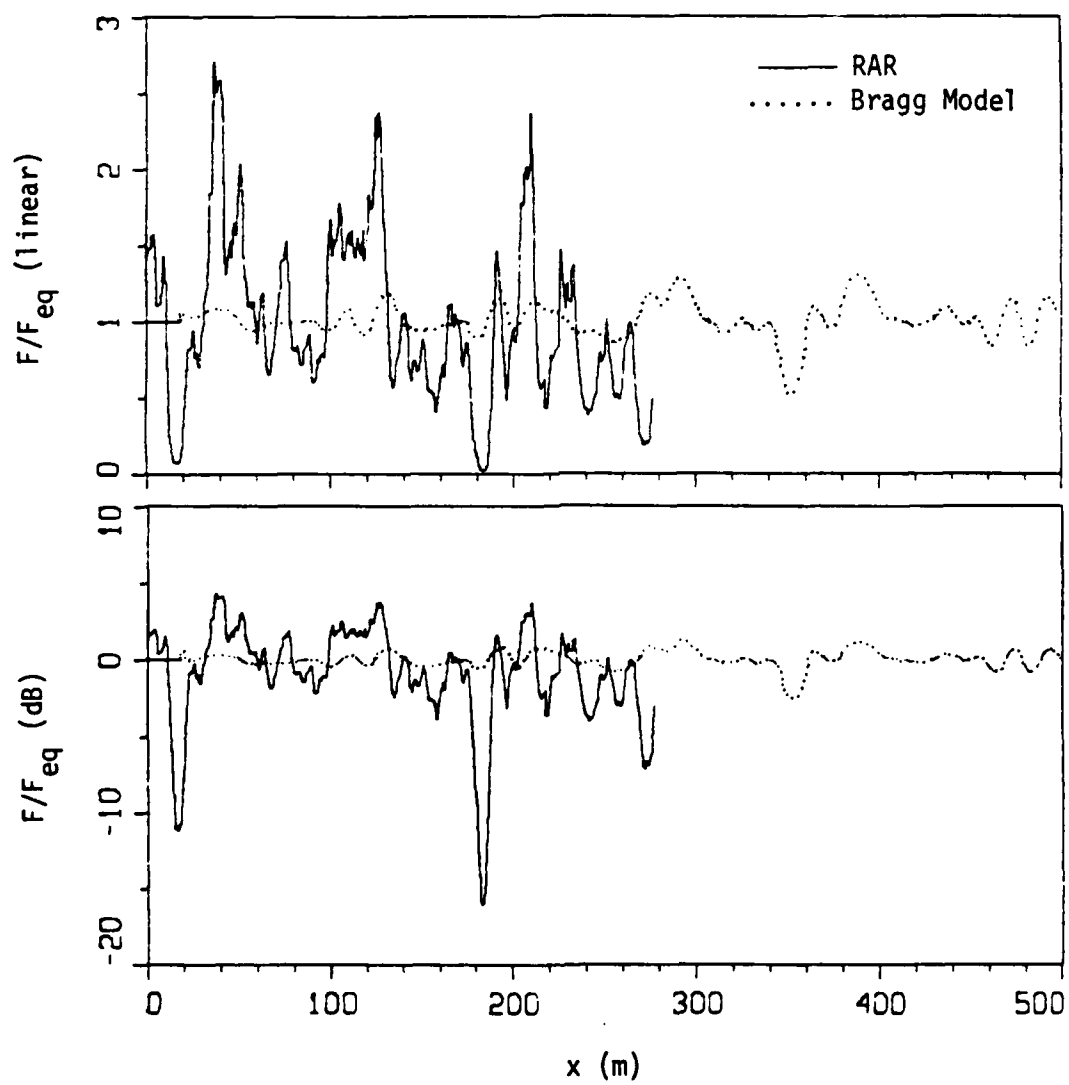


FIGURE 14

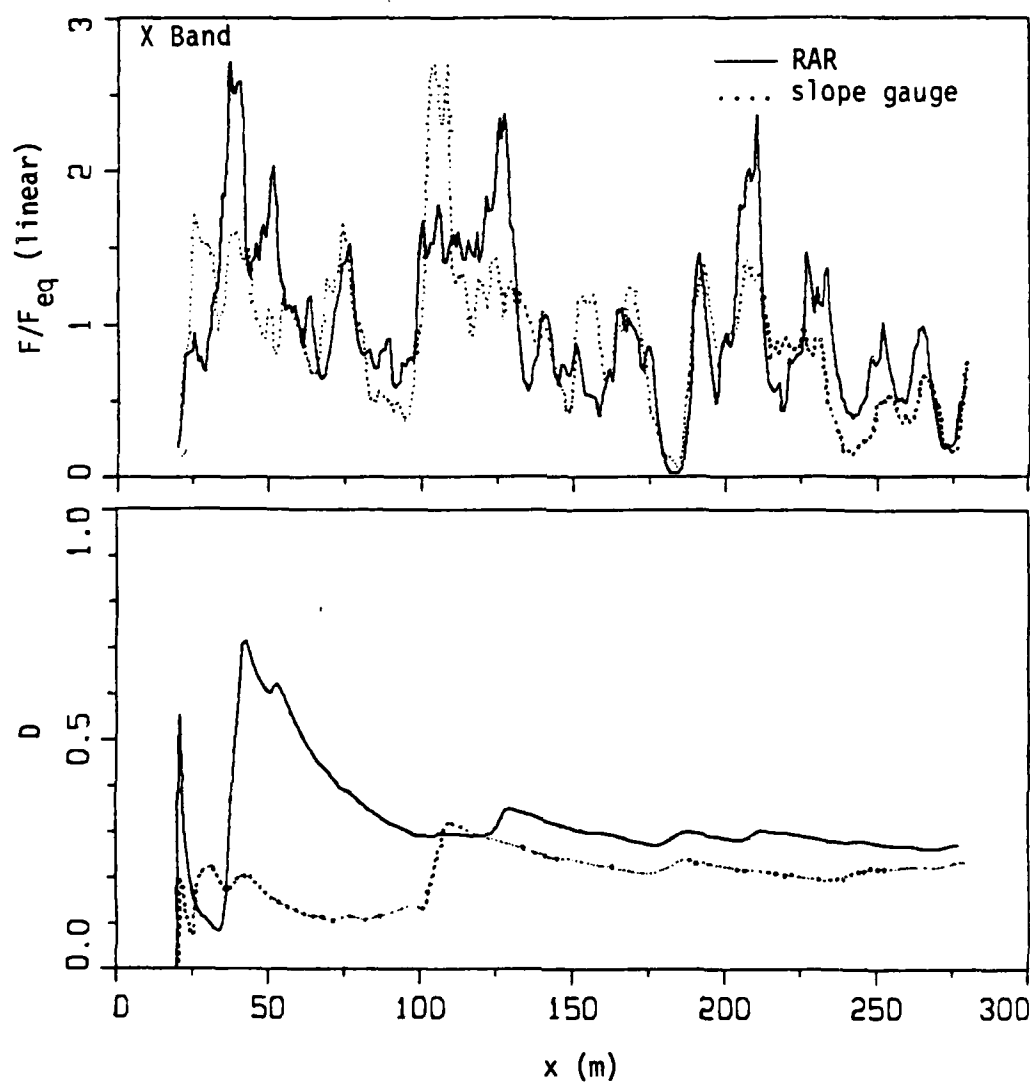


FIGURE 15

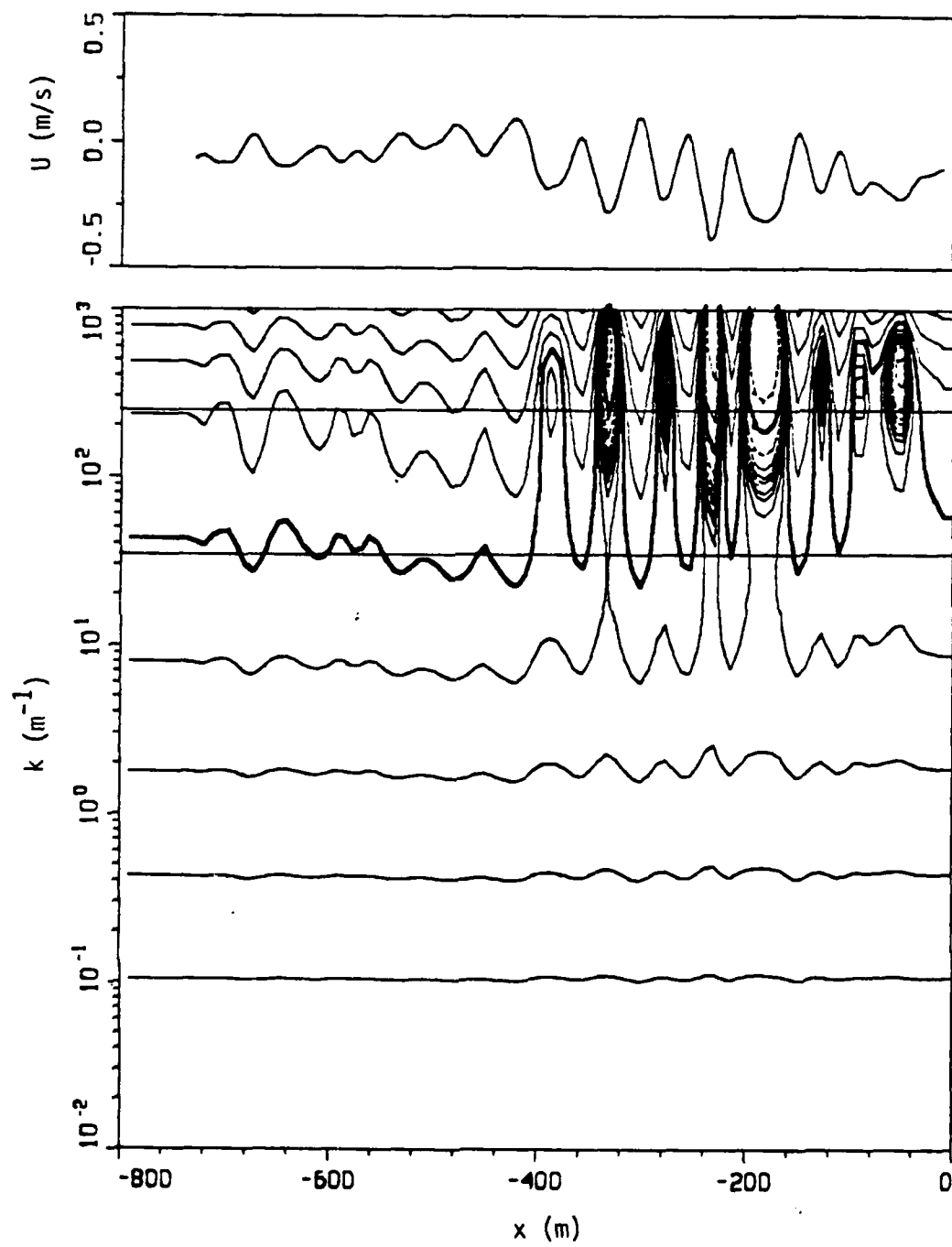


FIGURE 16

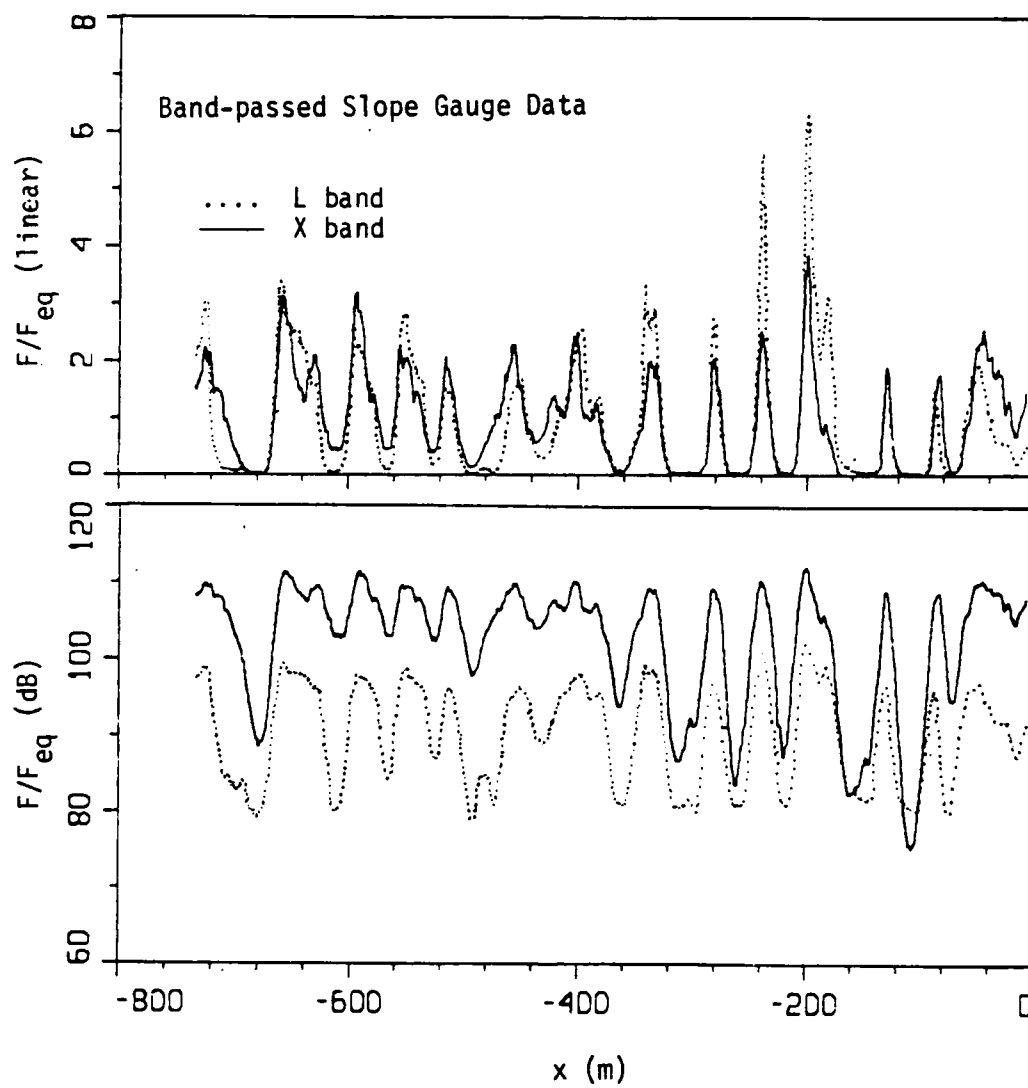


FIGURE 17

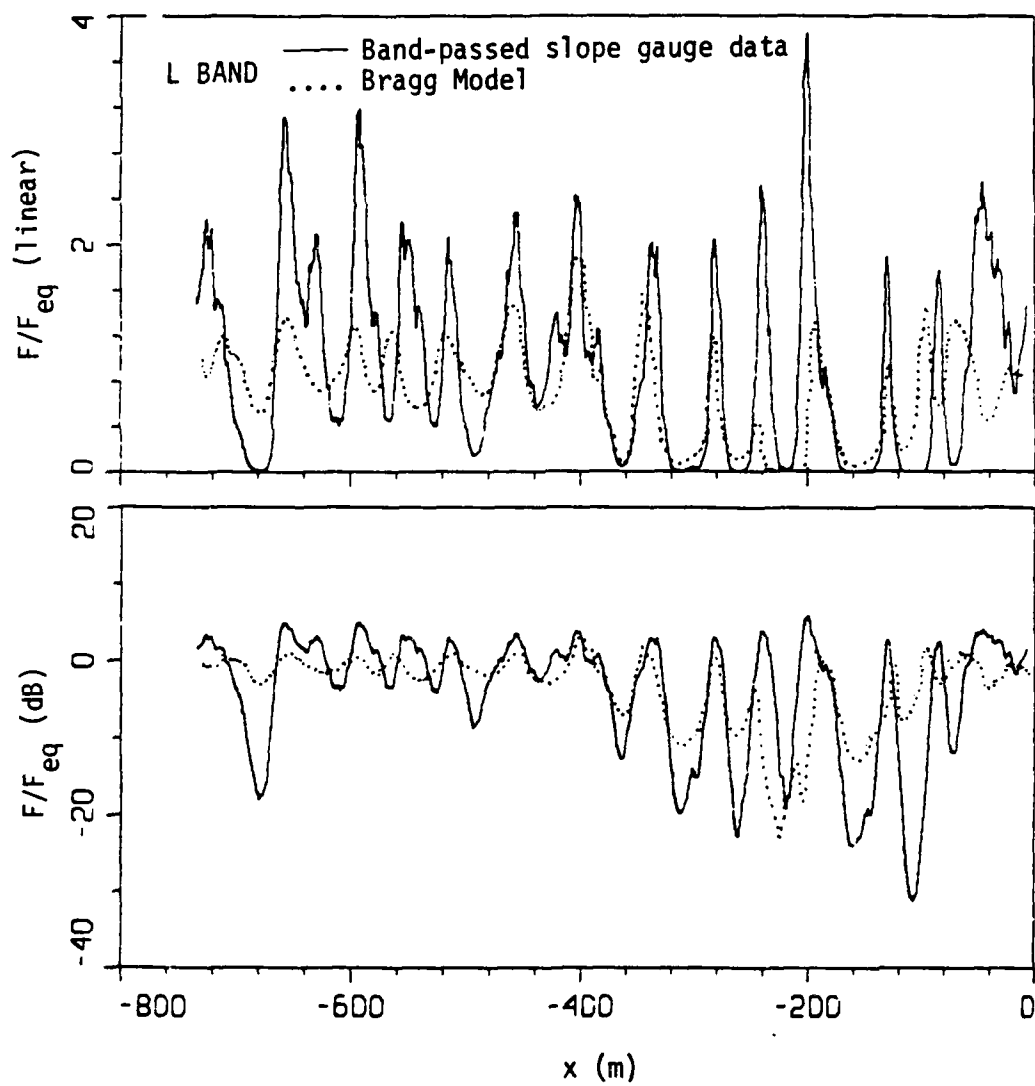


FIGURE 18

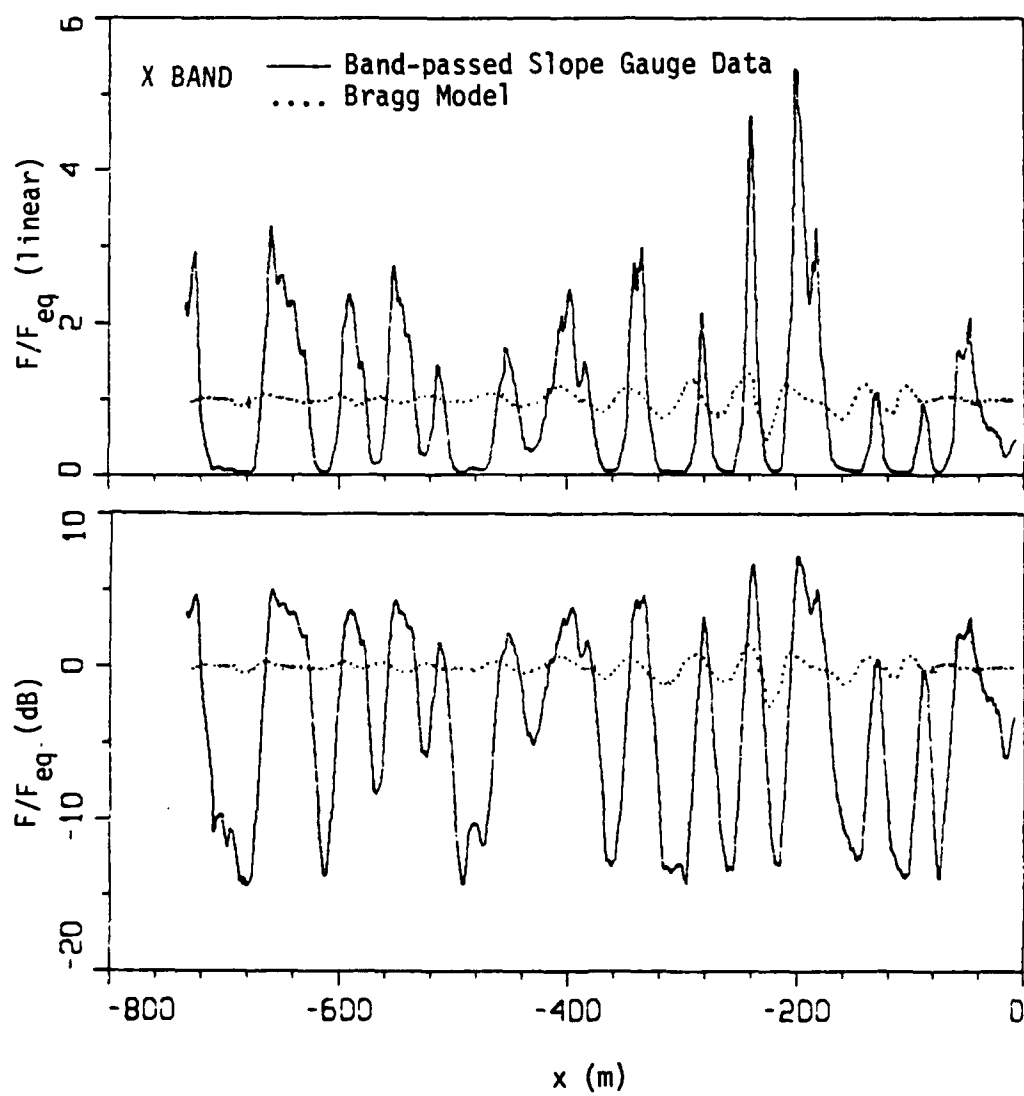


FIGURE 19

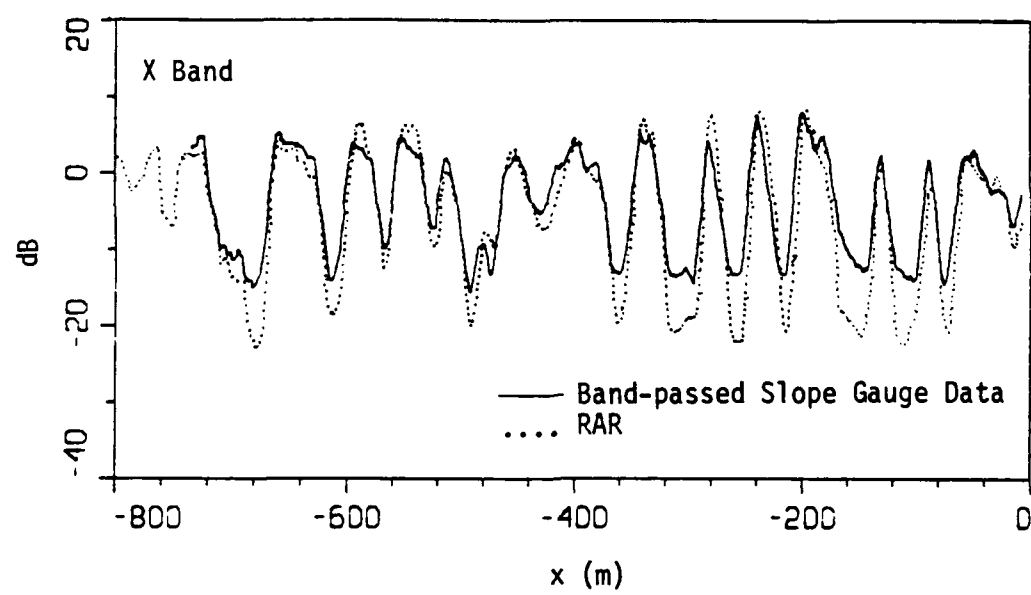


FIGURE 20

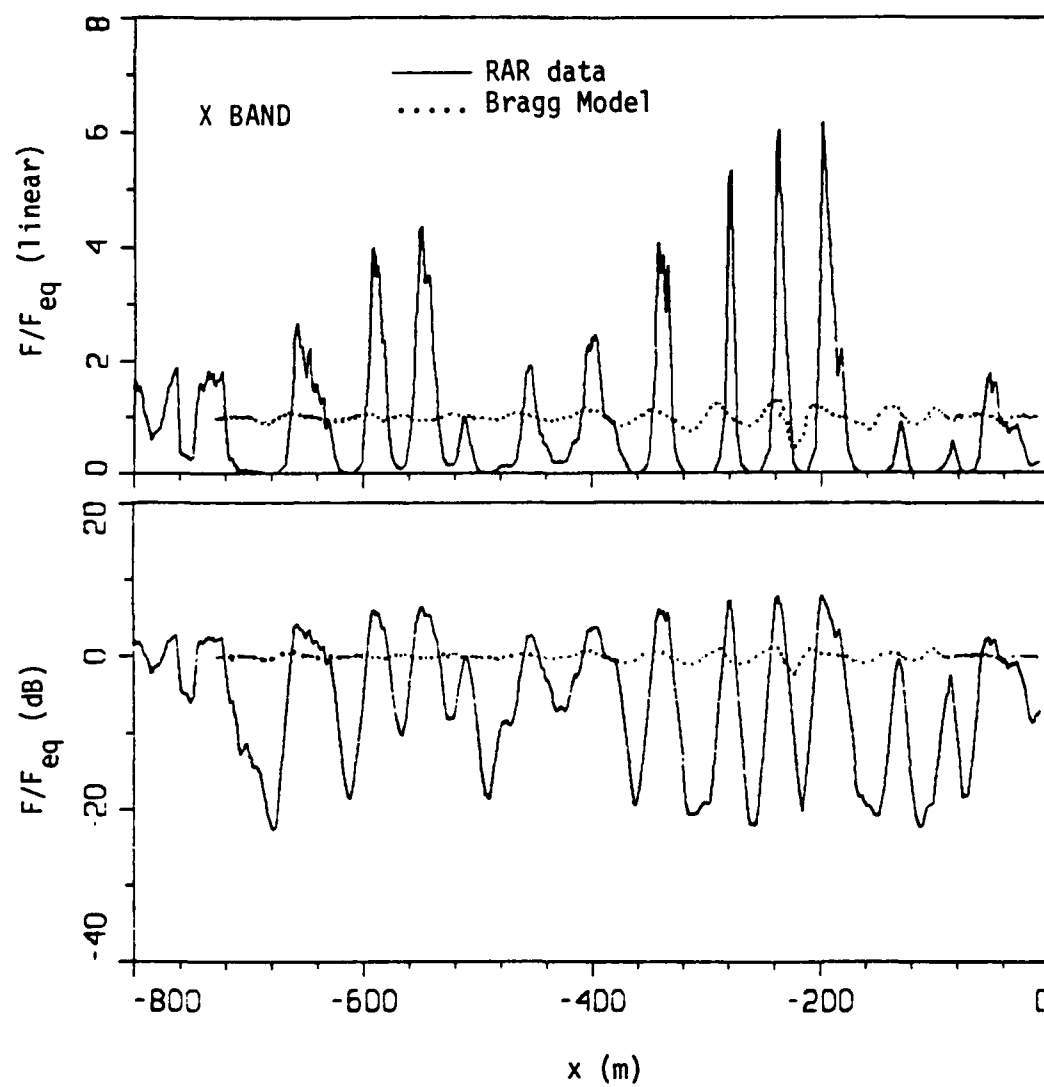


FIGURE 21

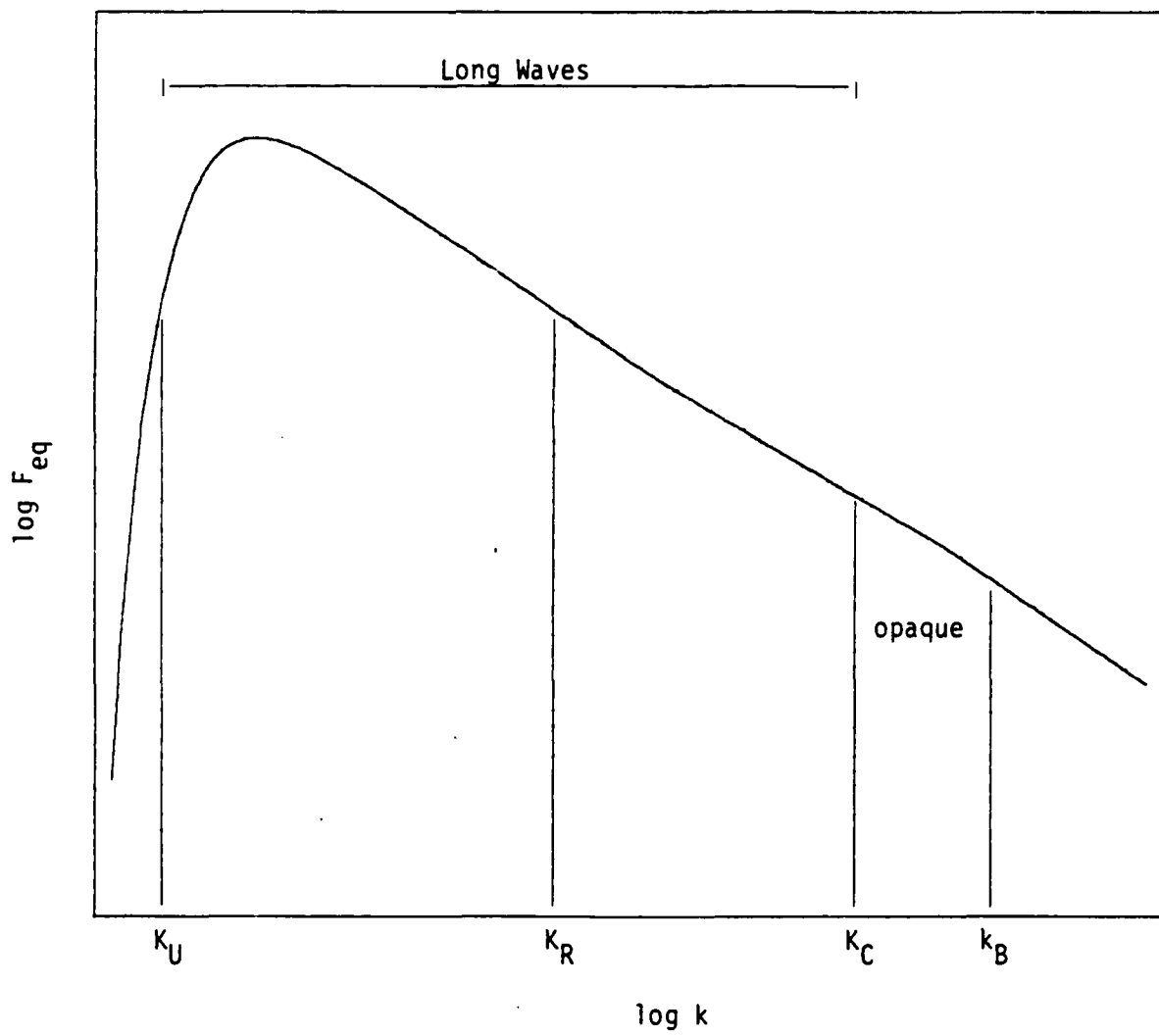


FIGURE 22

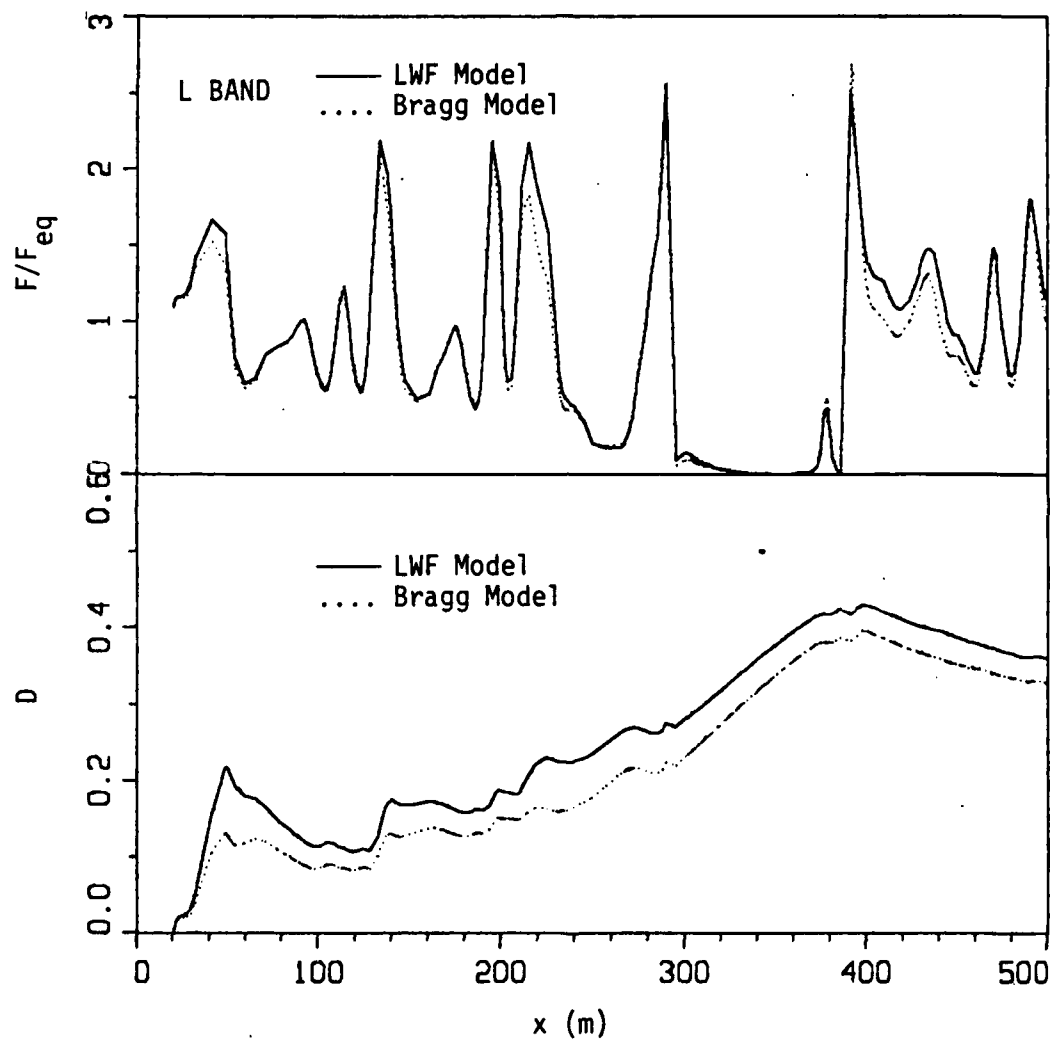


FIGURE 23

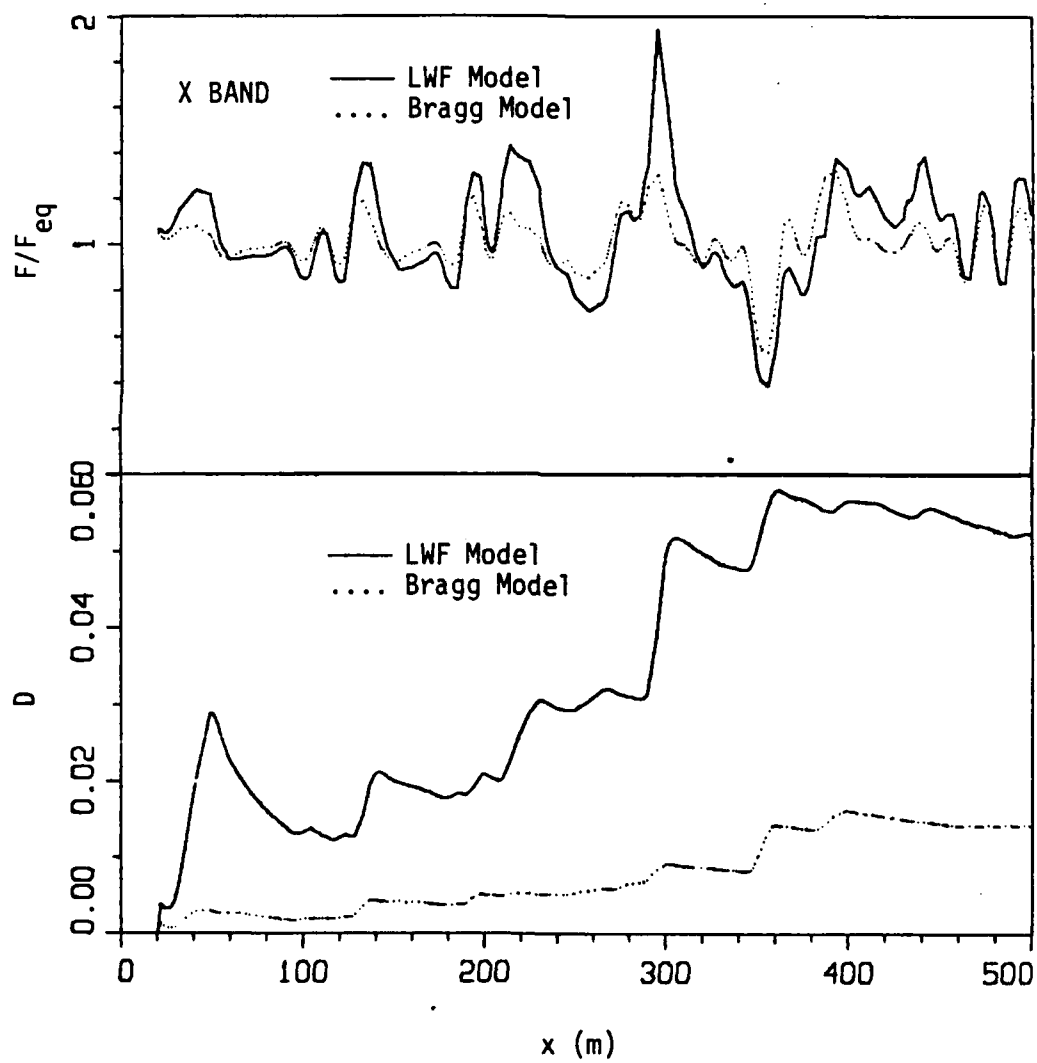


FIGURE 24

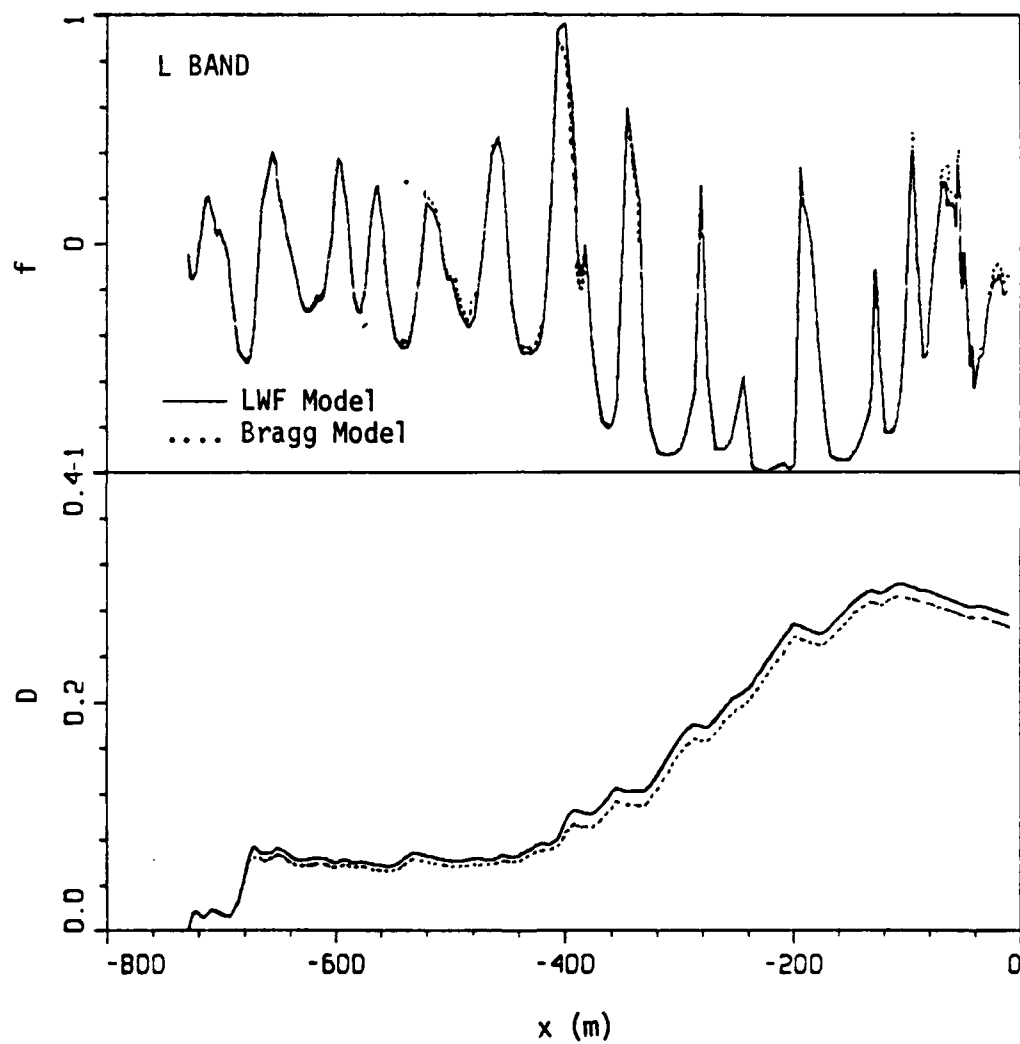


FIGURE 25

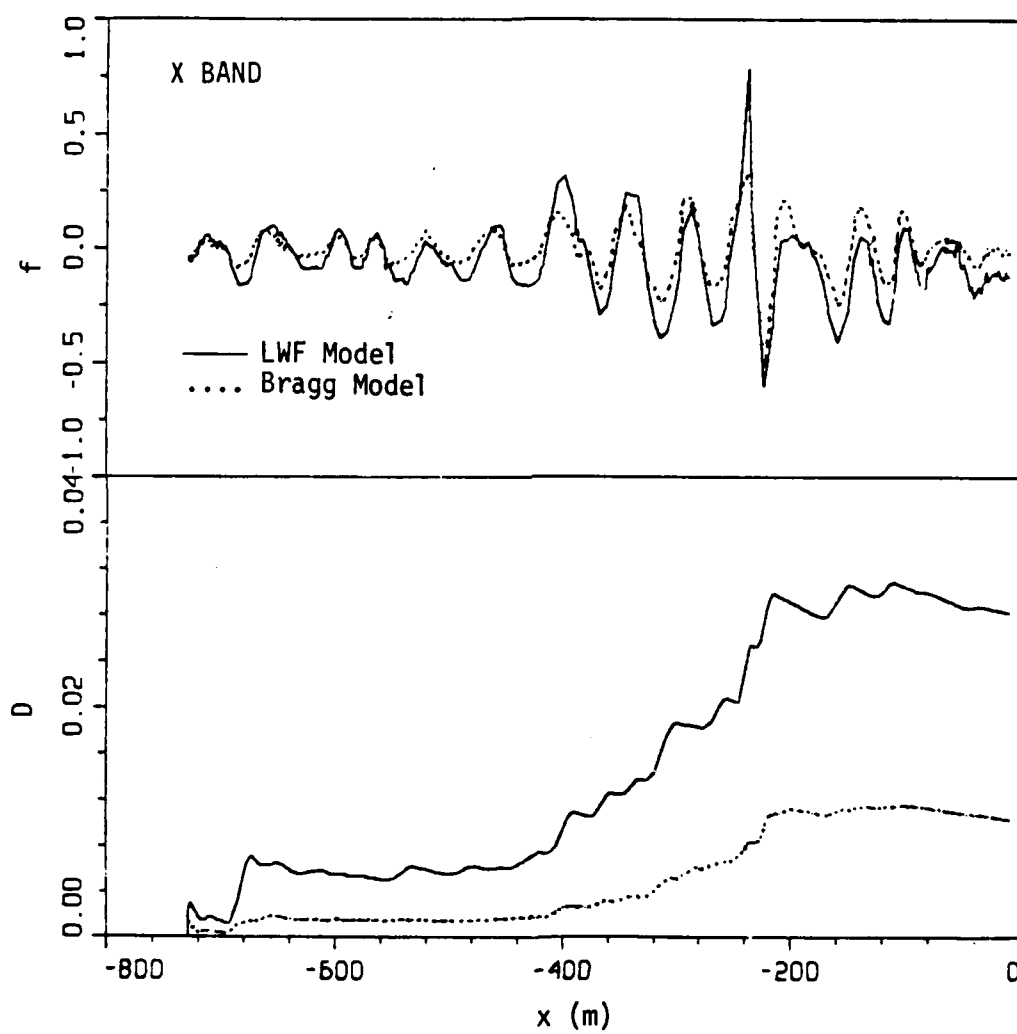


FIGURE 26

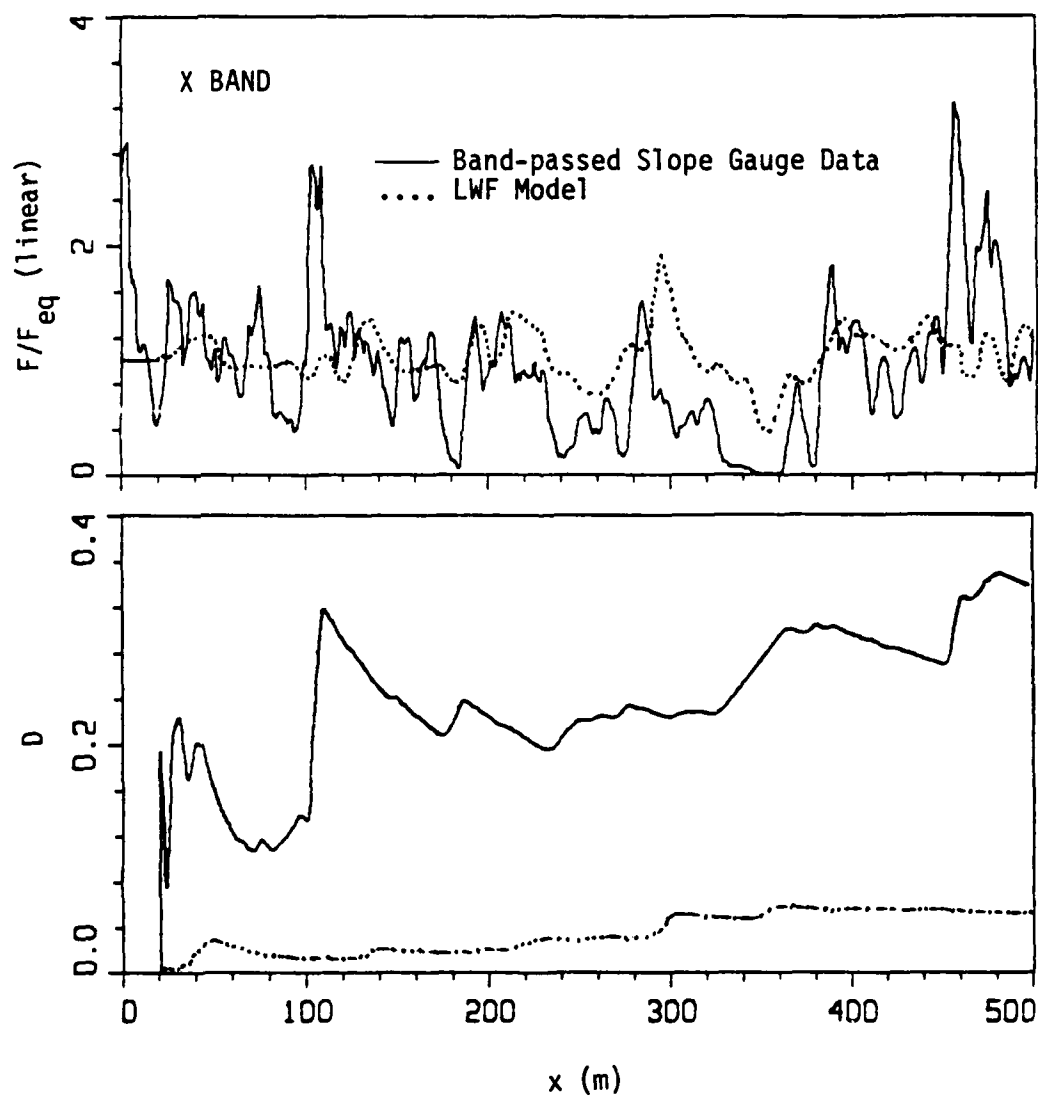


FIGURE 27

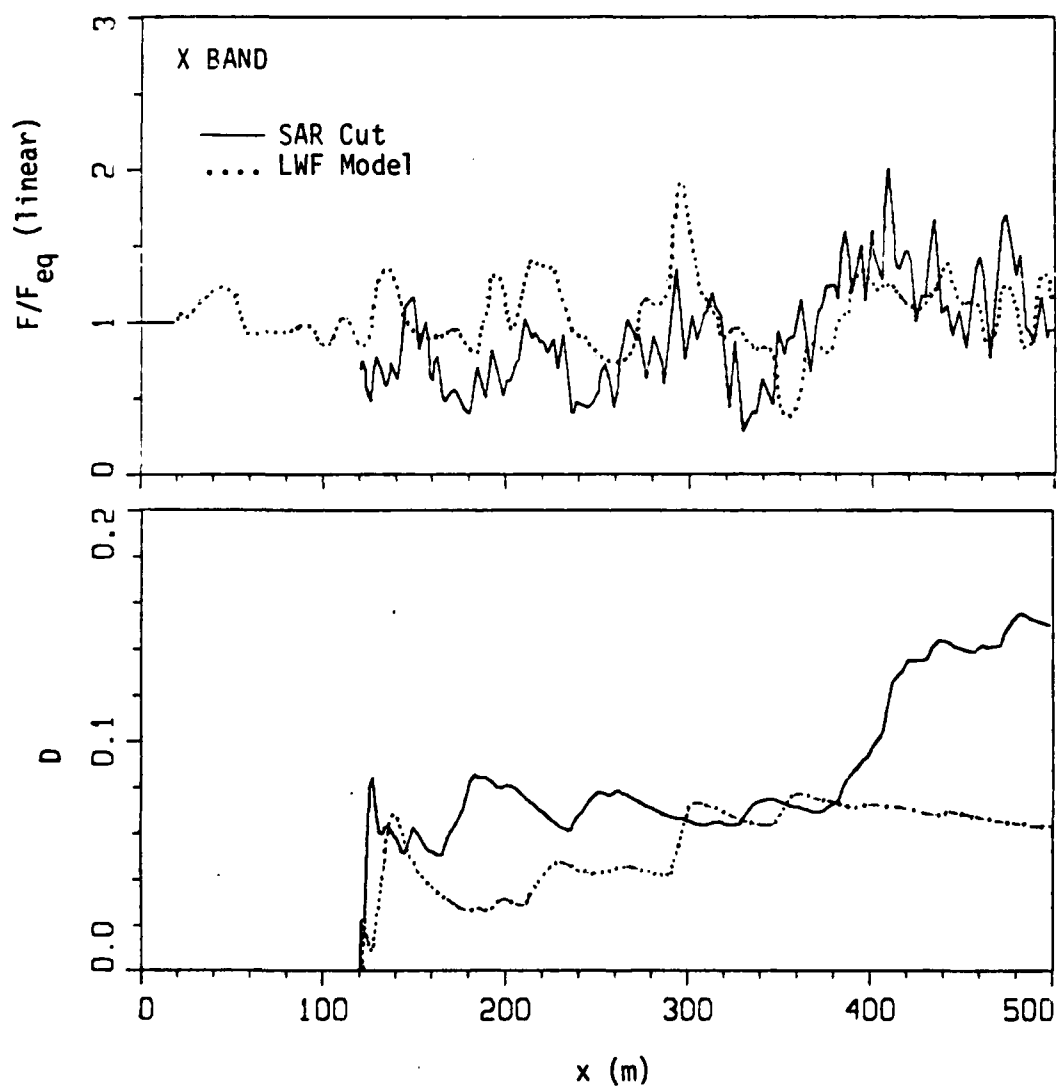


FIGURE 28

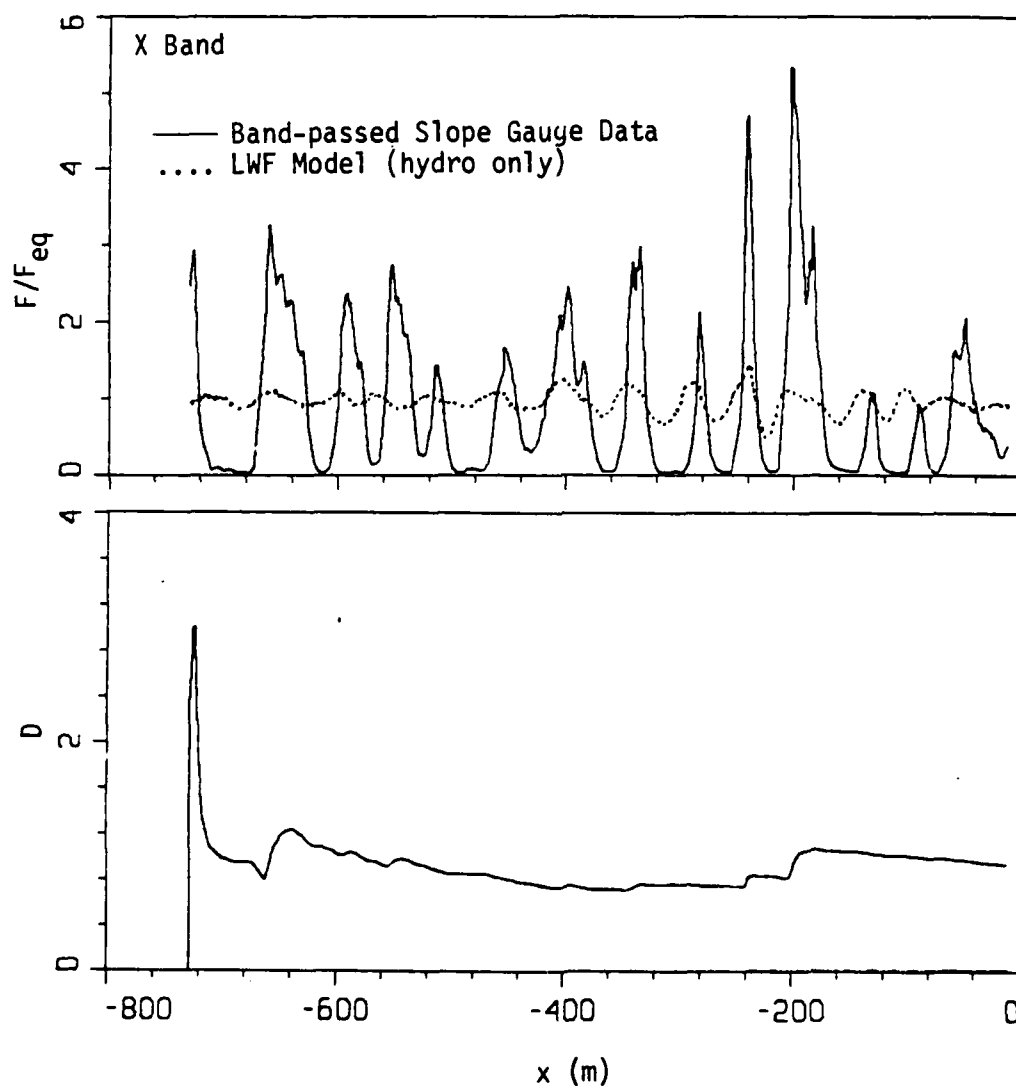


FIGURE 29

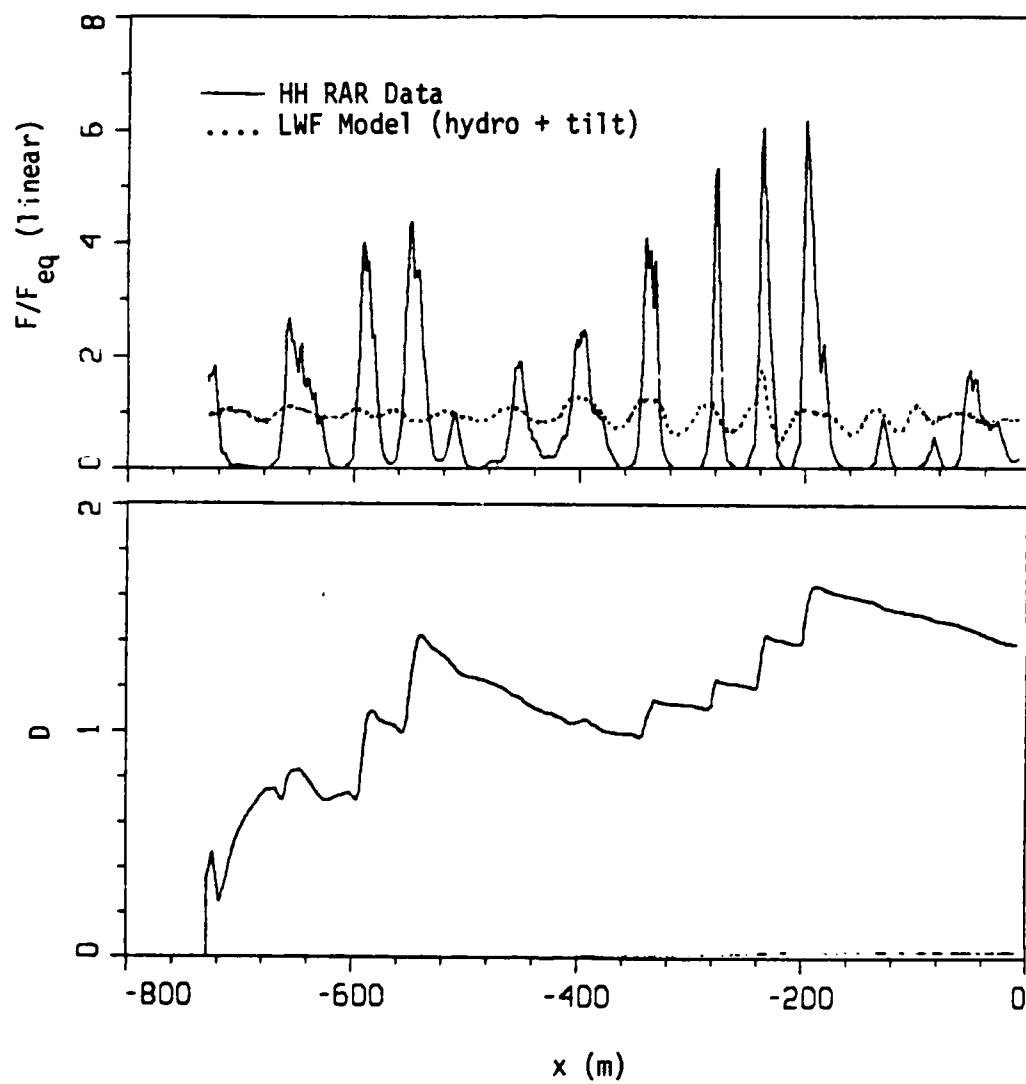


FIGURE 30